*Geol. Mag.* **154** (*1*), *2017, pp. 1–23.* © *Cambridge University Press 2015*
doi:10.1017/S0016756815000771


# Petrography and geochemistry of the siliciclastic Araba Formation (Cambrian), east Sinai, Egypt: implications for provenance, tectonic setting and source weathering

HOSSAM A. TAWFIK*†, IBRAHIM M. GHANDOUR*‡, WATARU MAEJIMA§, JOHN S. ARMSTRONG-ALTRIN¶ & ABDEL-MONEM T. ABDEL-HAMEED*

*Department of Geology, Faculty of Science, Tanta University, Tanta 31527, Egypt
‡Department of Marine Geology, Faculty of Marine Sciences, King Abdulaziz University, 80207 Jeddah 21589, Saudi Arabia
§Department of Geosciences, Graduate School of Science, Osaka City University, Sumiyoshi-ku, Osaka 558–8585, Japan
¶Universidad Nacional Autónoma de México, Instituto de Ciencias del Mar y Limnología, Unidad de Procesos Oceánicos y Costeros, Circuito exterior s/n, 04510 México D.F., México

(*Received* 13 April 2015; *accepted* 17 September 2015; *first published online* 17 November 2015)

**Abstract** – Combined petrographic and geochemical methods are utilized to investigate the provenance, tectonic setting, palaeo-weathering and climatic conditions of the Cambrian Araba clastic sediments of NE Egypt. The ~ 60 m thick Araba Formation consists predominantly of sandstone and mudstone interbedded with conglomerate. Petrographically the Araba sandstones are mostly sub-mature and classified as subarkoses with an average framework composition of $Q_{80}F_{14}L_6$. The framework components are dominated by monocrystalline quartz with subordinate K-feldspar, together with volcanic and granitic rock fragments. XRD analysis demonstrated that clay minerals comprise mixed-layer illite/smectite (I/S), illite and smectite, with minor kaolinite. Diagenetic features of the sandstone include mechanical infiltration of clay, mechanical and chemical compaction, cementation, dissolution and replacement of feldspars by carbonate cements and clays. The modal composition and geochemical parameters (e.g. Cr/V, Y/Ni, Th/Co and Cr/Th ratios) of the sandstones and mudstones indicate that they were derived from felsic source rocks, probably from the crystalline basement of the northern fringe of the Arabian–Nubian Shield. The study reveals a collisional tectonic setting for the sediments of the Araba Formation. Palaeo-weathering indices such as the chemical index of alteration (CIA), chemical index of weathering (CIW) and plagioclase index of alteration (PIA) of the clastic sediments suggest that the source area was moderately chemically weathered. On the northern margin of Gondwana, early Palaeozoic weathering occurred under fluctuating climatic conditions.

Keywords: Araba Formation, clay minerals, diagenesis, north Gondwana, Arabian–Nubian Shield, palaeoclimate.

## 1. Introduction

The petrography and geochemistry of siliciclastic sediments have been widely used to determine the degree of weathering (Nesbitt & Young, 1982; Fedo, Nesbitt & Young, 1995), source rock composition (Tawfik *et al.* 2011; Cao *et al.* 2012; Armstrong-Altrin *et al.* 2012, 2014), tectonic setting (Dickinson & Suczek, 1979; Bhatia, 1983; Verma & Armstrong-Altrin, 2013) and diagenesis (Zaid, 2015; Zaid & Gahtani, 2015; Zaid *et al.* 2015), as well as palaeogeographic reconstruction of provenance (Zimmermann & Spalletti, 2009; Armstrong-Altrin, 2015).

The siliciclastic-dominated Araba Formation, the lowermost Palaeozoic strata in Egypt, is widely distributed in NE Egypt. It crops out along a faulted zone along the foot slopes of Precambrian basement. The Araba Formation consists mainly of sandstone with mudstone and conglomerate intercalations. It varies in thickness from 5 to 130 m and seems to be barren of body fossils and, as a result, different ages have been suggested. The formation was assigned to the Early Cambrian by Omara (1972) and to the Cambrian by Said & El Kelani (1988).

The Araba Formation (Fig. 1) is coeval with the Mourizidie and Hassaouna formations in Libya, the Shifa Formation in the Western Desert, the Sarabit El-Khadim and Abu Hamata formations in SW Sinai (El Shahat & Kora, 1986), the fluvial Amudei Shelomo and the marine Timna and Shehoret formations in Israel, and the Salib, Burj, Um Ishrin and Disi formations in Jordan. It is also equivalent to the Siq and Saq formations in NW Arabia. This formation is believed to be an outcrop analogue to the subsurface 'Nubian D' unit, which is part of the Nubian reservoir that constitutes about 17 % of the hydrocarbon production in the Gulf of Suez region.

Although provenance studies are common, studies on the geochemistry of the siliciclastic sediments combined with petrographic data are meagre. Most of the

†Author for correspondence: hossam.abdelhameed@science.tanta.edu.eg

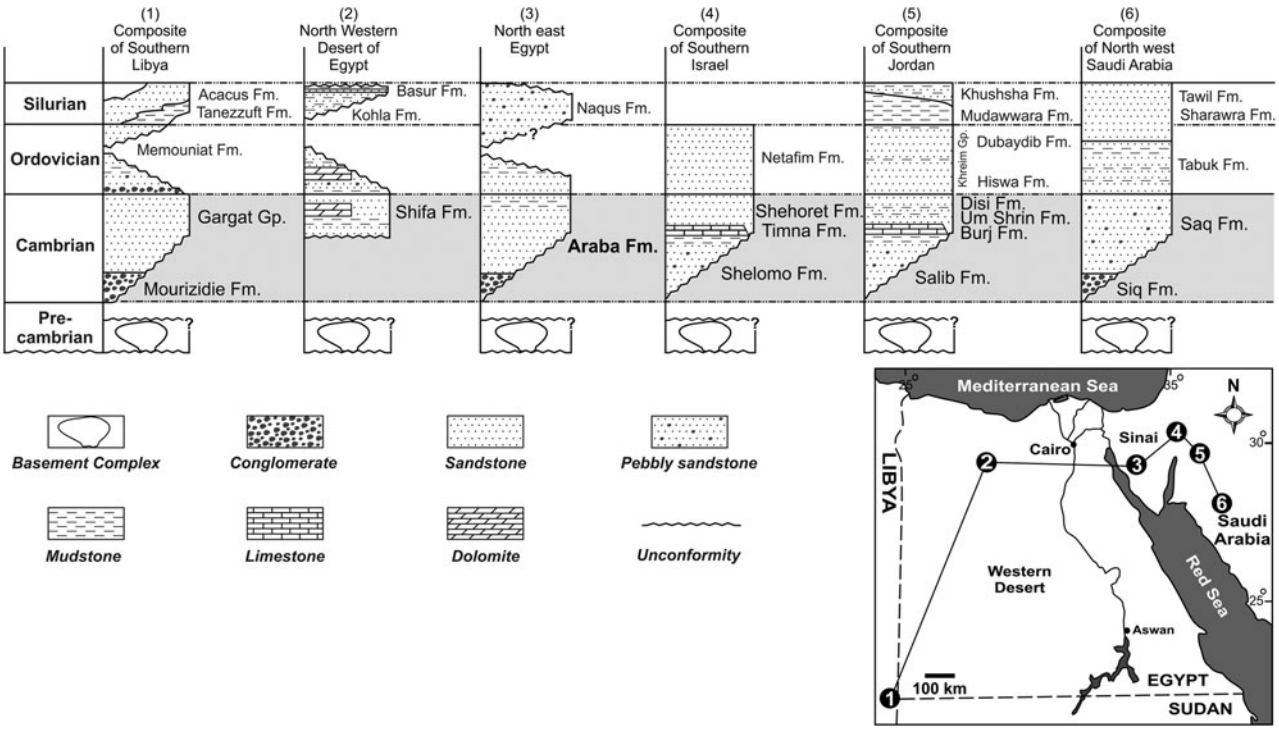


Figure 1. Correlation between the Cambrian rocks of Egypt and neighbouring countries. Adapted from (1) Bellini & Massa (1980); (2) Keeley (1989); (3) Issawi & Jux (1982); (4) Weissbrod & Perath (1990); (5) Lloyd (1968); and (6) (A. Al-Laboun, unpub. Ph.D. thesis, King Abdel-Aziz Univ. Saudi Arabia, 1982).

studies that have been carried out on the Araba Formation in NE Egypt have focused on its lithostratigraphy, facies analysis, depositional environment, sequence stratigraphy, diagenetic evolution and reservoir potential (Tawfik *et al.* 2010; Kordi, Turner & Salem, 2011; Ghandour *et al.* 2013). However, studies focused on provenance, tectonic setting and palaeo-weathering of the Araba Formation are very limited (e.g. Tawfik *et al.* 2011, 2012). In this paper, we examine the petrography, diagenetic features and geochemistry of the sandstones and mudstones of the Araba Formation exposed in the Taba area, east Sinai, Egypt. The objectives of this study are to document the diagenetic overprints, evaluate the source rock composition and tectonic setting, and to infer the palaeo-weathering and climatic conditions which prevailed during the deposition of the Araba clastic sediments.

## 2. Geological background

The Gondwana supercontinent, formed by the closure of the Mozambique Ocean and amalgamation of East and West Gondwana near the end of Neoproterozoic time, led to the formation of the East African Orogeny (EAO; Fig. 2). The EAO extends from southern Israel, Sinai and Jordan in the north to Mozambique and Madagascar in the south. Traditionally, it is subdivided into the Arabian–Nubian Shield (ANS) in the north, composed largely of juvenile Neoproterozoic crust (Fig. 2; Stern, 1994; Johnson *et al.* 2011), and the Mozambique Belt (MB) in the south, comprising mostly pre-Neoproterozoic crust with a Neoproterozoic – early Cambrian tectonothermal overprint.

The ANS is composed of accreted Neoproterozoic juvenile volcanic arcs, gneisses, metagabbros, metavolcano-sedimentary sequences, granites and gabbro–diorite complexes (Stern, 1994). At about 580–540 Ma, the ANS crust was stabilized, accompanied by continental-scale uplift, erosion and the development of intramountain basins and rifting (Moghazi, 2003; Avigad *et al.* 2005). At the end of Neoproterozoic time, the basement of North Africa and Arabia subsided thermally providing the accommodation space necessary for the deposition of platform-type Cambro-Ordovician fluvio-marine deposits that can be traced from Morocco in the west to Oman in the east (Avigad *et al.* 2005). These deposits thicken northwards and the sedimentation was accomplished by a continent-wide braided fluvial stream with a general south to north palaeocurrent direction throughout North Africa and Arabia. In this context, the overall North African palaeogeography during Cambrian time was that of a broad platform, gently sloping to the north and being progressively overstepped from north to south by a thin sedimentary veneer ranging southwards from shallow marine to fluvial (Ghienne *et al.* 2007).

The study area lies between latitudes 29° 31′–29° 33′ N and longitudes 34° 46′–34° 48′ E, along Wadi El-Khulayfiya to the west of the Gulf of Aqaba and Taba City, east Sinai, Egypt (Fig. 3). In this area, Precambrian basement of the ANS is nonconformably overlain by the Cambrian Araba Formation and the overlying Ordovician Naqus Formation. These siliciclastic deposits

https://doi.org/10.1017/S0016756815000771 Published online by Cambridge University Press

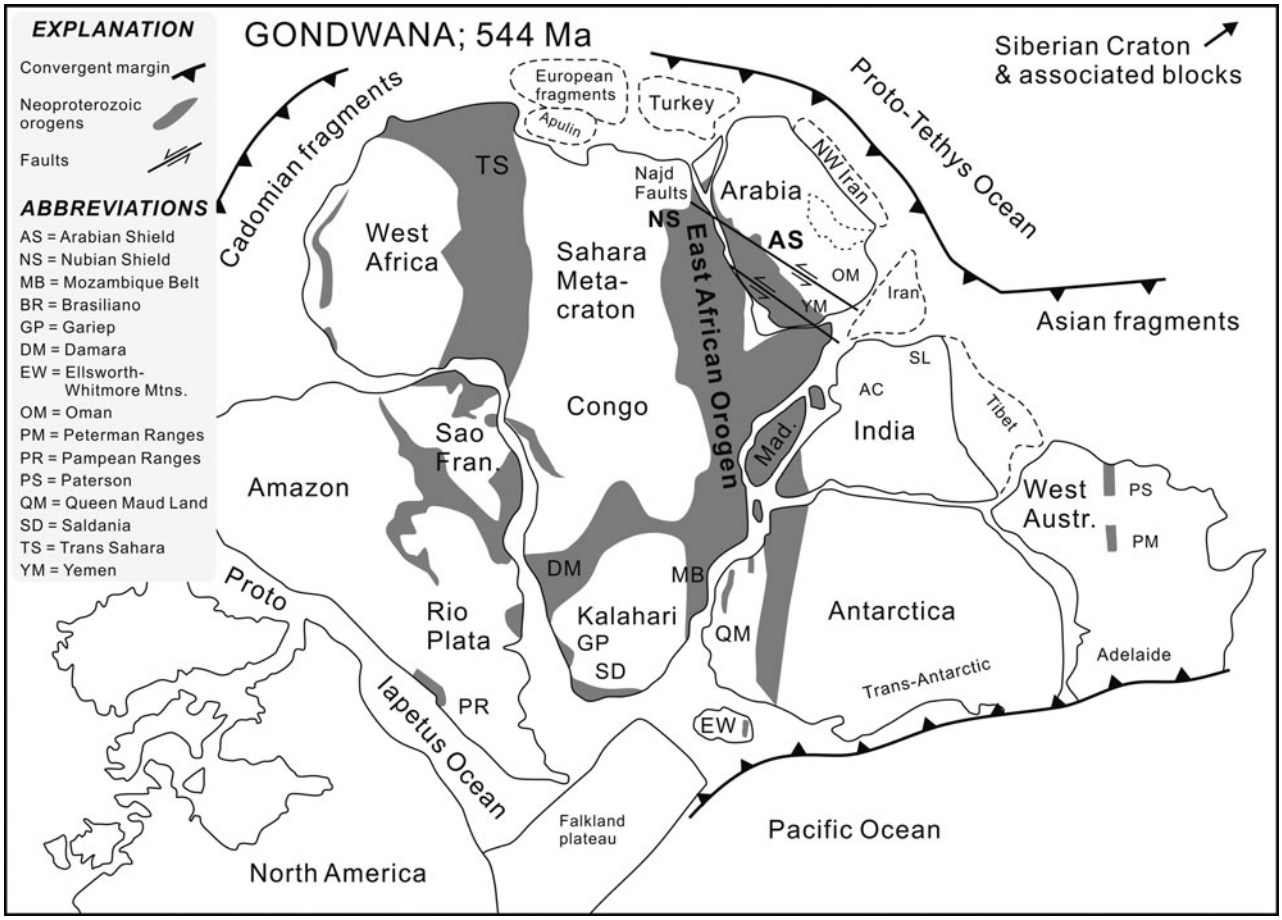


Figure 2. Map of Gondwana at the end of Neoproterozoic time showing the general arrangement of different tectonic elements (after Powell *et al.* 1994).

are unconformably succeeded by the Lower Cretaceous Malha Formation and the overlying Upper Cretaceous Galala, Wata and Matalla formations.

The Araba Formation attains a thickness of ~ 60 m in the study area and consists of very fine-grained to pebbly sandstone with mudstone, conglomerate and rare carbonate intercalations (Fig. 4). This formation was deposited in fluvio-marine environments and is differentiated into three incomplete depositional units. The basal one (Unit-I) is ~ 12 m of medium- to coarse-grained sandstones, arranged in seven vertically stacked 0.8 to 3 m thick channels that seem to have been deposited in a northward-flowing low-sinuosity braided fluvial system.

The second unit (Unit-II) is ~ 33 m of fining-upwards strata representing deposition in a fluvio-marine setting with an upwards increase in marine influence. It consists at the base of 15 m thick massive clast- to matrix-supported conglomerates grading upwards into alternating massive to horizontal-laminated sandstones and reddish brown mudstones. This basal part is interbedded with thin cross- and ripple-laminated fine-grained sandstone representing ephemeral flash flood and associated distal floodplain deposits. The middle part, on the other hand, is dominated by 6–12 m thick heterolithic reddish brown argillaceous fine-grained sandstones, interbedded with massive, plane parallel-laminated to cross-stratified medium-grained sandstones, and locally a thin dolomitic bed. These strata bear features such as tidal laminites, mud drapes, oppositely dipping cross-lamination, alternations of thick sand – thin mud couplets, reactivation surfaces, wave ripples and abundant vertical burrows suggesting deposition in an intertidal flat setting. The upper part of this unit is represented by ~ 10 m of mudstones interbedded with storm-induced thin wave-rippled to hummocky cross-stratified sandstones deposited in an offshore to offshore – lower shoreface transition environment. It is sharply capped by cross-stratified coarse-grained sandstones of upper shoreface affinity. The contact between Unit-II and Unit-III is defined by a ~ 1.5 m thick palaeosol representing a subaerial unconformity.

Unit-III (~ 16 m thick) is dominated by heterolithic deposits of intertidal flat origin, sharply and erosively overlain by thick-bedded and cross-stratified coarse-grained sandstones of shallow marine origin.

## 3. Material and methods

The mineralogical, petrographic and geochemical studies were carried out at the Department of Geosciences, Osaka City University in Japan.

https://doi.org/10.1017/S0016756815000771 Published online by Cambridge University Press

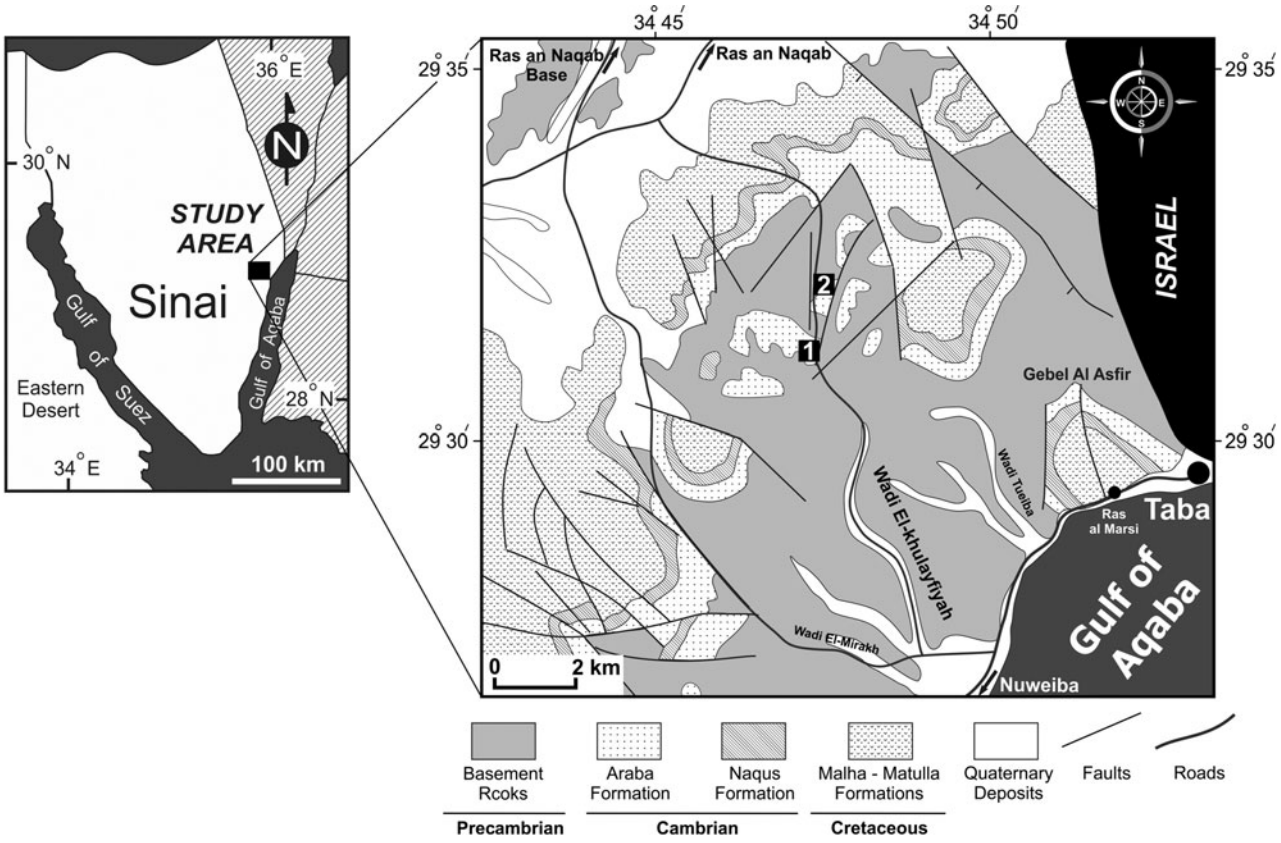


Figure 3. Simplified location and geological maps of the Taba region, west of the Gulf of Aqaba, NE Egypt. Numbers refer to the location of the measured sections.

A total of 65 sandstone and mudstone samples were collected from the entire Araba Formation. Among them 45 thin-sections were prepared. The selected sandstone samples were impregnated with blue-dye epoxy under vacuum to identify porosity and stained with Alizarin Red-S and potassium ferricyanide to facilitate mineral identification. The sandstone modal composition was quantified based on counting 500 points in each thin-section using the Gazzi-Dickinson method. Grain texture and fabric were visually identified by measuring the maximum diameter of 100 random grains per thin-section under the microscope.

The clay mineralogy of the mudstone and selected sandstone samples was determined by conventional X-ray diffraction (XRD) method, using smear-on-glass slide and powder press techniques. The samples were completely dispersed in a diluted solution of Calgon to avoid flocculation. The oriented mounts of clay fractions ($< 2\ \mu m$) were prepared by pipetting the clay suspension onto glass slides. The analysis was done by a RIGAKU RAD-I X-ray diffractometer (CuKα-radiation with 30 kV, 10 mA, 2–70° 2-theta). Discrimination between kaolinite and chlorite was done after heating the samples to 550 °C for two hours in a muffle furnace. Expandable clays were determined after treatment with ethylene glycol at 25 °C for 15 hours.

Fifteen sandstone samples were examined by a KEYENCE VE-7800 Scanning Electron Microscope (SEM) at 15 and 20 kV accelerating voltages for identification of delicate cementing materials. The chemical compositions of some selected silicate and carbonate minerals plus different cement types were obtained using a JEOL JSM-5500 SEM equipped with an EDAX-EDS system (CDU-LEAP and back-scattered electron (BSE) detectors and Genesis software). Operating conditions during electron microprobe analyses were an acceleration voltage of 20 kV and a beam current of 500 pA. The concentrations of Si, Ti, Al, Fe, Mn, Ca, Mg, Ba, N, K, P, Ni, Co, Cr, V, Cu and Zn were quantitatively measured.

Major- and trace-element concentrations of 45 sandstone and 9 mudstone samples were obtained by a RIGAKU RIX 2100 X-ray fluorescence spectrometer (XRF), equipped with a Rh/W dual-anode X-ray tube. The analyses were performed on the whole-rock specimens under a 50 kV and 50 mA accelerating voltage and tube current, respectively. Fused glass discs were prepared by mixing 1.8 g of powdered sample (dried to 110 °C for 4 hours), with 3.6 g of Spectroflux ($Li_2B_4O_7$ 20 %, $LiBO_2$ 80 %, dried at 450 °C for 4 hours), 0.54 g of oxidant $LiNO_3$ (dried at 110 °C for 4 hours) and traces of LiI. The mixture was fused at 800 °C for 120 sec and 1200 °C for 400 sec. The chemical index of alteration (CIA), chemical index of weathering (CIW) and plagioclase index of alteration (PIA) were calculated following the methods of Nesbitt & Young (1982),

https://doi.org/10.1017/S0016756815000771 Published online by Cambridge University Press

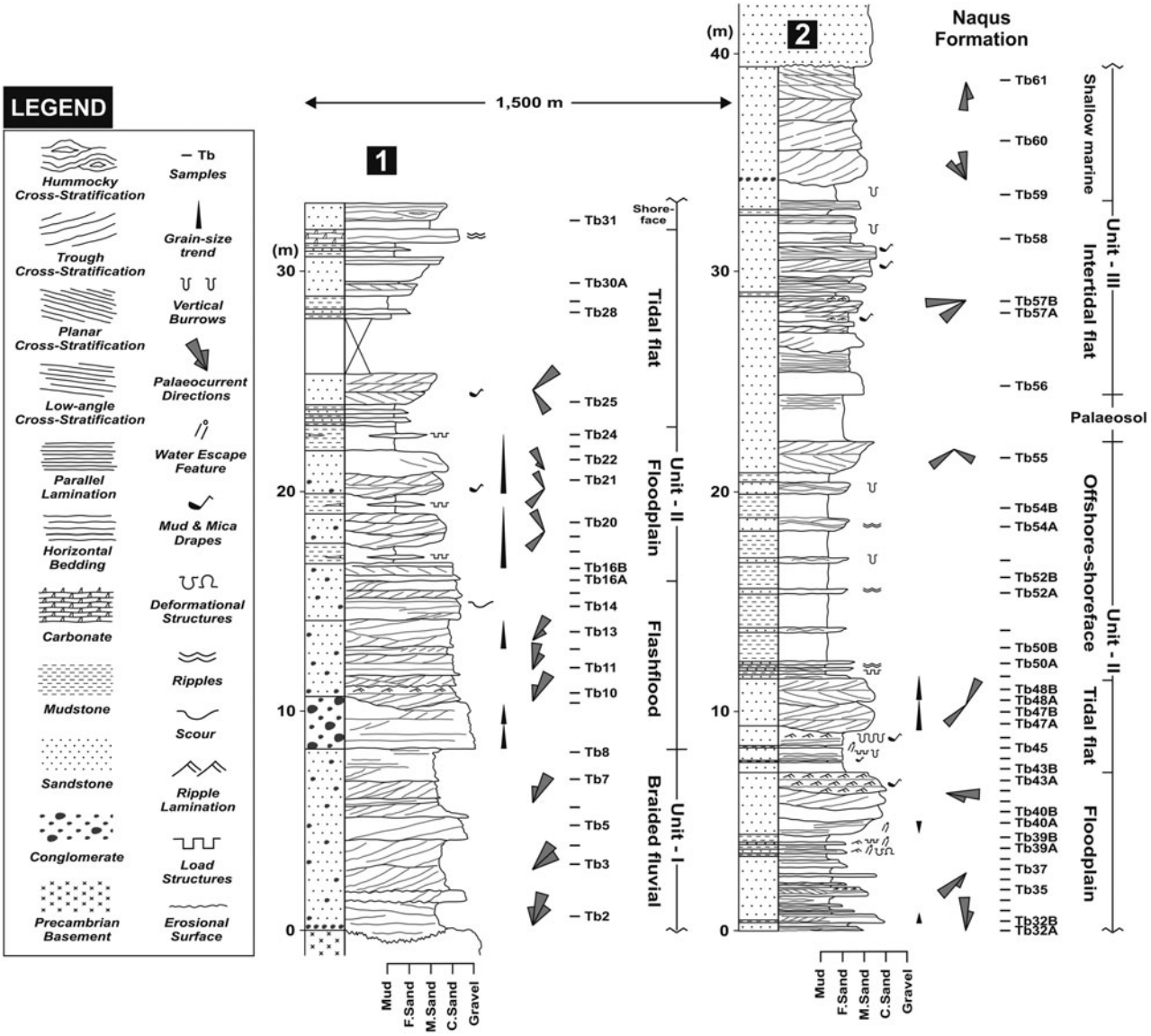


Figure 4. Measured sections (1 and 2) and the proposed depositional settings of the studied Araba sandstones exposed in the Taba region, east Sinai, Egypt.

Harnois (1988) and Fedo, Nesbitt & Young (1995), respectively.

## 4. Results

### 4.a. Petrography

#### *4.a.1. Conglomerate*

Clast- to matrix-supported conglomerate is a minor lithofacies found in the basal part of the Araba Formation of the study area (Fig. 4). The conglomerates have polymictic composition with dominantly granite, volcanic, quartz and chert pebbles. Clasts are up to 20 cm in length, sub-angular to rounded in shape and poorly sorted. They yield N–NW palaeocurrent directions. Sandstone matrix clasts are sub-angular to sub-rounded, moderately to well sorted and consist of quartz, lithic fragments and rarely K-feldspar that is cemented by iron oxides, silica and clay cements.

#### *4.a.2. Sandstone*

The sandstones of the Araba Formation are composed mainly of framework grains (average 75 %), diagenetic cements (av. 18.6 %) and porosity (av. 6.4 %) with a minor amount of matrix. They vary from very fine to very coarse grained and poorly to very well sorted with angular to rounded grains (Table 1). The extrabasinal non-carbonate grains are represented mainly by monocrystalline and polycrystalline quartz (av. 49.1 % and 9.2 %, respectively; Table 1). Monocrystalline grains mostly display straight to slightly undulose extinction and occasionally contain mineral inclusions such as zircon and tourmaline crystals, and rarely rutile needles (Fig. 5a). Some monocrystalline quartz grains are

https://doi.org/10.1017/S0016756815000771 Published online by Cambridge University Press

Table 1. Textural parameters and modal composition of the Araba Formation

| Sample No. | Granulometric Parameters | | | Detrital Mineralogy | | | | | | | | | Cementing Materials | | | | | | | | Porosity Tp |
|---|---|---|---|---|---|---|---|---|---|---|---|---|---|---|---|---|---|---|---|---|---|
| | Grain Size | Sorting | Roundness | Qm | Qp | Qt | F | L | M | Hm | Mc | Mtx | Cly | Fe | $Q_{ov}$ | $Fd_{ov}$ | Crb | Br | Apt | Tpf | Trc | |
| Tb61 | F* sand | VWS | Sub-rounded | 51.2 | 9.6 | 60.8 | 12.0 | 1.6 | 0.0 | 2.4 | 0.0 | 0.0 | 9.4 | 0.4 | 0.0 | 0.0 | 0.0 | 0.0 | 0.0 | 9.8 | 0.6 | 12.8 |
| Tb60 | M sand | MWS | Sub-rounded | 50.8 | 13.0 | 63.8 | 8.2 | 0.6 | 0.2 | 0.4 | 0.0 | 0.0 | 14.0 | 0.0 | 0.8 | 0.0 | 0.0 | 0.4 | 0.0 | 15.2 | 0.8 | 10.8 |
| Tb59 | F*-VF* sand | MWS | Sub-rounded | 54.0 | 4.8 | 58.8 | 10.0 | 2.8 | 3.8 | 0.4 | 0.0 | 0.0 | 14.6 | 0.0 | 0.0 | 0.0 | 0.0 | 0.0 | 0.0 | 14.6 | 0.2 | 9.4 |
| Tb54A | F* sand | VWS | Sub-angular | 56.8 | 8.4 | 65.2 | 8.0 | 1.2 | 0.4 | 0.8 | 0.0 | 0.0 | 6.6 | 0.0 | 0.0 | 0.0 | 0.0 | 0.0 | 0.0 | 6.6 | 0.4 | 17.4 |
| Tb52A | F* sand | WS | Sub-rounded | 64.8 | 8.8 | 73.6 | 10.8 | 1.6 | 0.2 | 0.0 | 0.0 | 0.0 | 6.2 | 0.0 | 1.6 | 0.0 | 0.0 | 0.4 | 0.0 | 8.2 | 0.6 | 5.0 |
| Tb50A | F* sand | VWS | Sub-rounded | 55.2 | 5.6 | 60.8 | 7.6 | 1.2 | 1.0 | 0.6 | 0.0 | 0.0 | 1.6 | 0.0 | 20.8 | 0.0 | 0.0 | 0.6 | 0.0 | 23.0 | 0.2 | 5.6 |
| Tb48A | M-C sand | M-PS | Rounded | 47.6 | 9.2 | 56.8 | 14.4 | 4.0 | 0.2 | 0.4 | 4.4 | 0.0 | 2.8 | 0.4 | 1.8 | 0.2 | 6.8 | 1.0 | 0.0 | 13.0 | 0.6 | 6.2 |
| Tb47A | F*-M sand | WS | Rounded | 49.6 | 14.8 | 64.4 | 12.2 | 0.8 | 0.0 | 0.2 | 0.0 | 0.0 | 4.2 | 0.2 | 0.0 | 0.0 | 0.0 | 0.0 | 0.0 | 4.4 | 1.2 | 16.8 |
| Tb46 | VF* sand | VWS | Angular | 55.8 | 2.0 | 57.8 | 18.0 | 1.2 | 0.8 | 0.6 | 0.0 | 0.0 | 20.6 | 0.2 | 0.0 | 0.0 | 0.0 | 0.0 | 0.0 | 20.8 | 0.0 | 0.8 |
| Tb45 | F* sand | WS | Sub-rounded | 63.0 | 5.0 | 68.0 | 8.2 | 1.4 | 0.0 | 1.4 | 0.0 | 0.0 | 9.0 | 0.0 | 0.2 | 0.0 | 0.0 | 0.0 | 2.6 | 11.8 | 1.8 | 10.0 |
| Tb44 | F*-M sand | VWS | Sub-rounded | 56.0 | 9.8 | 65.8 | 14.2 | 2.0 | 0.0 | 0.2 | 0.0 | 0.0 | 2.0 | 0.0 | 0.8 | 0.0 | 0.0 | 0.0 | 0.0 | 2.8 | 0.8 | 14.2 |
| Tb43A | VF* sand | VWS | Sub-angular | 58.2 | 1.2 | 59.4 | 19.8 | 0.8 | 3.2 | 0.4 | 0.0 | 0.0 | 8.6 | 0.6 | 0.0 | 0.0 | 0.0 | 0.0 | 0.0 | 9.2 | 1.2 | 6.0 |
| Tb42 | F*-VF* sand | MWS | Angular | 50.6 | 0.8 | 51.4 | 4.4 | 0.4 | 8.4 | 0.0 | 0.0 | 0.0 | 27.0 | 8.0 | 0.2 | 0.0 | 0.0 | 0.0 | 0.0 | 35.2 | 0.0 | 0.2 |
| Tb41 | VF* sand | VWS | Angular | 46.8 | 5.0 | 51.8 | 15.8 | 0.2 | 2.2 | 0.2 | 0.0 | 0.0 | 17.0 | 1.4 | 0.4 | 0.0 | 0.0 | 0.0 | 0.0 | 18.8 | 0.8 | 10.2 |
| Tb40A | VF* sand | VWS | Sub-angular | 47.6 | 1.8 | 49.4 | 11.2 | 0.4 | 0.2 | 0.0 | 0.0 | 0.0 | 3.0 | 2.2 | 0.0 | 0.0 | 30.2 | 0.0 | 0.0 | 35.4 | 1.8 | 1.6 |
| Tb39A | VF* sand | WS | Angular | 45.6 | 3.6 | 49.2 | 9.0 | 2.4 | 0.4 | 0.0 | 0.0 | 0.0 | 21.6 | 0.6 | 0.0 | 0.0 | 15.8 | 0.0 | 0.0 | 38.0 | 0.2 | 0.8 |
| Tb38 | VF* sand | VWS | Sub-angular | 57.2 | 1.8 | 59.0 | 8.0 | 0.0 | 7.2 | 0.6 | 0.0 | 0.0 | 9.6 | 8.4 | 0.0 | 0.0 | 6.2 | 0.0 | 0.0 | 24.2 | 0.2 | 0.8 |
| Tb37 | VF* sand | VWS | Sub-angular | 40.0 | 2.6 | 42.6 | 9.8 | 0.0 | 30.0 | 0.0 | 0.0 | 0.0 | 10.6 | 6.6 | 0.0 | 0.0 | 0.0 | 0.0 | 0.0 | 17.2 | 0.0 | 0.4 |
| Tb36 | F* sand | WS | Sub-rounded | 61.4 | 4.4 | 65.8 | 11.2 | 1.0 | 0.8 | 0.8 | 0.0 | 0.0 | 13.4 | 0.4 | 3.8 | 0.0 | 0.0 | 0.4 | 0.0 | 18.0 | 0.6 | 1.8 |
| Tb34 | F*-VF* sand | MWS | Sub-angular | 40.2 | 2.0 | 42.2 | 10.4 | 1.0 | 1.8 | 0.6 | 0.0 | 0.0 | 16.8 | 24.8 | 0.0 | 0.0 | 0.0 | 0.0 | 0.0 | 41.6 | 0.0 | 2.4 |
| Tb33 | VF* sand | VWS | Sub-angular | 52.2 | 4.4 | 56.6 | 17.2 | 1.0 | 0.0 | 0.4 | 0.0 | 0.0 | 5.2 | 0.4 | 0.0 | 0.0 | 0.0 | 0.0 | 0.0 | 5.6 | 0.4 | 18.8 |
| Tb32A | VF* sand | WS | Sub-angular | 53.6 | 1.4 | 55.0 | 20.2 | 0.4 | 1.2 | 0.2 | 0.0 | 0.0 | 10.2 | 9.8 | 0.0 | 0.0 | 0.0 | 0.0 | 0.0 | 20.0 | 0.8 | 2.2 |
| Tb30A | F* sand | WS | Sub-rounded | 45.0 | 3.6 | 48.6 | 13.6 | 2.2 | 2.6 | 0.2 | 0.0 | 0.0 | 11.4 | 1.0 | 1.2 | 0.0 | 0.0 | 0.0 | 0.0 | 13.6 | 1.2 | 18.0 |
| Tb28 | F*-VF* sand | WS | Sub-rounded | 42.0 | 1.4 | 43.4 | 9.4 | 1.0 | 0.8 | 0.2 | 0.0 | 0.0 | 2.2 | 3.8 | 0.2 | 0.0 | 37.0 | 0.4 | 0.0 | 43.6 | 1.6 | 0.0 |
| Tb25 | VF* sand | WS | Sub-angular | 46.0 | 2.4 | 48.4 | 16.6 | 0.0 | 0.0 | 0.6 | 0.0 | 0.0 | 1.4 | 1.2 | 0.0 | 0.0 | 27.6 | 0.0 | 0.0 | 30.2 | 1.0 | 3.2 |
| Tb24 | F*-M sand | WS | Rounded | 52.2 | 5.4 | 57.6 | 11.2 | 2.0 | 0.4 | 0.0 | 0.0 | 0.0 | 6.8 | 0.2 | 1.0 | 0.0 | 18.4 | 0.0 | 0.0 | 26.4 | 0.8 | 1.6 |
| Tb22 | F*-C sand | PS | Sub-rounded | 52.4 | 7.6 | 60.0 | 10.6 | 12.2 | 2.2 | 0.2 | 0.2 | 0.0 | 1.6 | 0.0 | 3.6 | 0.2 | 0.0 | 2.0 | 0.0 | 7.4 | 0.6 | 5.4 |
| Tb21 | M-C sand | MWS | Rounded | 42.6 | 11.0 | 53.6 | 6.8 | 8.4 | 0.0 | 0.2 | 0.0 | 0.0 | 1.6 | 0.0 | 0.0 | 0.0 | 28.4 | 0.0 | 0.0 | 30.0 | 0.6 | 0.4 |
| Tb20 | M-C sand | WS | Sub-rounded | 44.6 | 12.2 | 56.8 | 1.2 | 8.4 | 0.0 | 0.0 | 0.0 | 0.0 | 0.8 | 1.6 | 0.0 | 0.0 | 30.6 | 0.0 | 0.0 | 33.0 | 0.6 | 0.0 |
| Tb18 | M-C sand | MS | Sub-rounded | 57.8 | 3.8 | 61.6 | 10.6 | 3.8 | 0.2 | 0.0 | 0.0 | 0.0 | 3.0 | 0.0 | 2.2 | 0.0 | 0.0 | 0.0 | 0.0 | 5.2 | 0.2 | 18.4 |
| Tb16B | F*-VC sand | MS | Rounded | 54.6 | 10.4 | 65.0 | 10.4 | 1.8 | 0.0 | 0.4 | 0.0 | 0.0 | 1.6 | 18.6 | 0.8 | 0.0 | 0.0 | 0.0 | 0.2 | 21.2 | 0.0 | 1.2 |
| Tb16A | VC sand | PS | Rounded | 24.8 | 25.0 | 49.8 | 4.0 | 34.0 | 0.0 | 0.0 | 0.0 | 0.8 | 2.8 | 2.6 | 2.4 | 0.0 | 0.0 | 0.0 | 0.0 | 7.8 | 0.4 | 3.2 |
| Tb15 | M-C sand | MWS | Sub-rounded | 49.6 | 25.2 | 74.8 | 6.6 | 0.6 | 0.8 | 0.6 | 0.0 | 0.0 | 6.2 | 2.6 | 0.2 | 0.0 | 0.0 | 0.0 | 0.0 | 9.0 | 0.0 | 7.6 |
| Tb14 | M-C sand | MS | Sub-angular | 50.8 | 19.8 | 70.6 | 6.4 | 3.2 | 0.8 | 0.0 | 0.0 | 0.0 | 4.4 | 7.4 | 0.2 | 0.0 | 0.4 | 0.0 | 0.0 | 12.4 | 0.2 | 5.8 |
| Tb12 | C-VC sand | MWS | Sub-rounded | 42.6 | 22.0 | 64.6 | 6.8 | 0.0 | 0.8 | 0.2 | 0.0 | 0.2 | 4.2 | 8.4 | 1.4 | 0.0 | 0.0 | 0.0 | 0.0 | 14.0 | 0.2 | 13.2 |

Table 1. Continued

| Sample No. | Granulometric Parameters | | | Detrital Mineralogy | | | | | | | | Cementing Materials | | | | | | | | Porosity |
|---|---|---|---|---|---|---|---|---|---|---|---|---|---|---|---|---|---|---|---|---|
| | Grain Size | Sorting | Roundness | Qm | Qp | Qt | F | L | M | Hm | Mc | Mtx | Cly | Fe | $Q_{ov}$ | $Fd_{ov}$ | Crb | Br | Apt | Tpf | Trc | Tp |
| Tb11 | VC sand | PS | Rounded | 16.2 | 12.4 | 28.6 | 3.6 | 49.4 | 0.0 | 0.0 | 0.0 | 0.0 | 0.8 | 8.2 | 4.2 | 0.0 | 0.0 | 0.0 | 0.0 | 13.2 | 0.0 | 5.2 |
| Tb10 | F*-M sand | WS | Sub-angular | 48.6 | 7.0 | 55.6 | 13.6 | 1.2 | 0.2 | 0.0 | 0.0 | 0.0 | 22.0 | 4.6 | 0.4 | 0.0 | 0.0 | 0.0 | 0.0 | 27.0 | 0.6 | 1.8 |
| Tb9 | M sand | WS | Sub-rounded | 54.8 | 11.8 | 66.6 | 9.4 | 0.6 | 0.2 | 0.2 | 0.0 | 0.8 | 9.8 | 6.8 | 1.0 | 0.0 | 0.0 | 0.0 | 0.0 | 17.6 | 1.0 | 3.6 |
| Tb8 | VC sand | PS | Rounded | 31.4 | 26.2 | 57.6 | 7.8 | 19.0 | 0.4 | 0.0 | 0.0 | 1.0 | 5.6 | 1.0 | 2.0 | 0.0 | 0.0 | 0.0 | 0.0 | 8.6 | 0.0 | 5.6 |
| Tb7 | M-C sand | WS | Sub-angular | 51.0 | 10.8 | 61.8 | 15.4 | 1.4 | 0.6 | 0.2 | 0.0 | 0.0 | 13.6 | 3.4 | 0.4 | 0.0 | 0.8 | 0.0 | 0.0 | 18.2 | 0.2 | 2.0 |
| Tb6 | VC sand | MWS | Rounded | 48.6 | 13.6 | 62.2 | 9.6 | 2.6 | 0.2 | 0.4 | 0.0 | 0.0 | 7.0 | 5.8 | 0.2 | 0.0 | 0.0 | 0.0 | 0.0 | 13.0 | 0.0 | 12.0 |
| Tb5 | C-VC sand | M-PS | Sub-rounded | 50.8 | 21.0 | 71.8 | 5.2 | 2.4 | 0.0 | 0.0 | 0.0 | 0.0 | 3.2 | 8.4 | 0.0 | 0.0 | 0.0 | 0.0 | 4.2 | 15.8 | 0.0 | 4.8 |
| Tb4 | M-C sand | MS | Sub-angular | 46.1 | 16.4 | 62.5 | 13.0 | 1.2 | 0.2 | 0.3 | 0.0 | 0.0 | 9.6 | 8.4 | 0.2 | 0.0 | 0.0 | 0.0 | 0.0 | 18.2 | 0.0 | 4.6 |
| Tb3 | M sand | WS | Sub-rounded | 49.6 | 6.6 | 56.2 | 8.6 | 1.2 | 0.0 | 0.4 | 0.2 | 0.0 | 14.4 | 10.0 | 0.2 | 0.0 | 2.6 | 0.0 | 0.0 | 27.2 | 0.0 | 6.2 |
| Tb2 | M-C sand | WS | Sub-rounded | 51.2 | 16.8 | 68.0 | 10.4 | 1.0 | 0.2 | 0.4 | 0.0 | 0.0 | 7.0 | 0.0 | 0.8 | 0.0 | 0.4 | 0.0 | 0.0 | 8.2 | 0.2 | 11.6 |
| Average | | | | 49.1 | 9.2 | 58.3 | 10.5 | 4.1 | 1.6 | 0.3 | 0.1 | 0.1 | 8.3 | 3.7 | 1.2 | 0.0 | 4.6 | 0.1 | 0.2 | 18.1 | 0.5 | 6.4 |

**Abbreviations:** VC – very coarse grained; C – coarse grained; M – medium grained; F* – fine grained; VF – very fine grained; VWS – very well sorted; WS – well sorted; MWS – moderately well sorted; MS – moderately sorted; PS – poorly sorted; Qm – monocrystalline quartz; Qp – polycrystalline quartz; Qt – total quartz; F – feldspar; L – rock fragment; M – mica; Hm – heavy minerals; Mc – mud clast; Mtx – matrix; Cly – clay mineral cements; Fe – iron-oxide cements; $Q_{ov}$ – quartz overgrowth; $Fd_{ov}$ – feldspar overgrowth; Crb – carbonate cements; Br – barite cement; Apt – apatite cement; Tpf – total pore-filling cement; Trc – total replacement cement; Tp, total porosity.

embayed and euhedral in shape. Polycrystalline quartz grains predominate in the coarse sand fraction and include subcrystals with straight, curved, sutured and crenulated intercrystalline boundaries.

Feldspars are second in abundance (av. 10.5 %; Table 1) and dominated by twinned K-varieties (e.g. microcline and perthite) that are partly to extensively altered to clay minerals. Rock fragments range from ~ 0 to 49.4 % (av. 4.1 %; Table 1) and are medium to very coarse and sub-angular to well rounded in shape. They are of igneous (av. 67 % of total lithic grains), sedimentary (av. 20 %) and metamorphic origin (av. 13 %). Grains made of volcanic rocks such as rhyolite and dacite are common (Fig. 5b) and coarse granitic and granophyre fragments are also dominant (Fig. 5c). Sedimentary grains are sub-rounded to well rounded and composed of unfossiliferous chert fragments. Metamorphic fragments are represented only by quartzite grains.

Muscovite and biotite (av. 1.6 %) are common in the Fe-rich, very fine- to fine-grained sandstones and occur as very fine comminute flakes and shreds. Mica flakes tend to be aligned parallel to bedding planes and deformed when sandwiched between detrital grains. Heavy minerals (av. 0.3 %) include zircon, tourmaline and rutile together with minor hornblende and apatite grains (Fig. 5d, e). Opaques are principally made of Fe and Ti varieties (Table 2). Intrabasinal non-carbonate grains are only represented by illitized mud intraclasts (av. 0.1 %) that are extensively compacted into a pseudomatrix (av. 0.1 %; Table 1).

On average, the present modal composition $Q_{80}F_{14}L_6$ suggests that the Araba sandstones are mainly subarkoses (McBride, 1963; Fig. 6). However, the present composition slightly differs from that at the time of deposition, which was probably $Q_{78}F_{16}L_6$, based on the abundance of mouldic pores, as well as macropores filled with cement (cf. McBride, 1977). These sandstones plot within the craton interior and transitional continental, as well as recycled orogenic fields (Dickinson *et al.* 1983; Fig. 7).

### 4.b. Clay mineralogy

XRD analysis of the sandstone and mudstone samples revealed no obvious qualitative difference in the mineralogical composition between the bulk and fine (< 2 μm) fractions. Clays are represented mainly by mixed-layer illite/smectite (I/S), illite and smectite, together with traces of kaolinite.

Mixed-layer I/S is the most abundant clay species, showing a broad diffraction peak between the basal spacing normally shown by its pure components. It constitutes about 46 % of the clay volume. Illite comprises about 32 % of the total clay volume and is characterized by 10.06, 5.00 and 3.35Å reflections. Smectite (montmorillonite) constitutes about 17 % of the total clay volume and is characterized by 14.6Å reflection. Unlike other clay species, kaolinite occurrence is restricted to the middle and upper layers of the Araba Formation.

https://doi.org/10.1017/S0016756815000771 Published online by Cambridge University Press

Table 2. Representative results of electron microprobe analyses in the Araba sandstones

| | Heavy Minerals | | | Authigenic Minerals | | | | | | |
|---|---|---|---|---|---|---|---|---|---|---|
| Minerals<br>Sample No. | Rutile<br>Tb51 | Hornblende<br>Tb7 | Fe-Ti Oxide<br>Tb3 | Illite<br>Tb9 | Kaolinite<br>Tb61 | Calcite<br>Tb25 | Dolomite<br>Tb28 | K-feldspar<br>Tb48B | Barite<br>Tb36 | Apatite<br>Tb5 |
| $SiO_2$ | 1.17 | 40.57 | 3.5 | 58.32 | 51.26 | 1.33 | 1.58 | 64.82 | 9.99 | 9.87 |
| $TiO_2$ | 95.60 | 1.86 | 31.5 | 0.14 | 0.23 | 0.66 | 0.7 | 0.26 | 3.87 | 1.06 |
| $Al_2O_3$ | 0.72 | 32.54 | 1.1 | 26.21 | 46.48 | 0.81 | 2.04 | 19.34 | 0.48 | 4.08 |
| FeO | 0.54 | 9.65 | 61.6 | 3.95 | 0.34 | 0.65 | 0.91 | 0.36 | 0.72 | 6.72 |
| MnO | 0.29 | 0.52 | - | - | 0.20 | 0.46 | 2.99 | 0.30 | 0.60 | 0.76 |
| CaO | 0.24 | 3.16 | - | 0.41 | 0.15 | 91.7 | 30.69 | 0.27 | 0.69 | 39.82 |
| MgO | 0.47 | 8.28 | 1.2 | 4.38 | 0.64 | 1.02 | 55.51 | 0.24 | 0.45 | 1.86 |
| BaO | - | - | - | - | 0.21 | - | - | 0.17 | 80.91 | - |
| $Na_2O$ | 0.32 | 1.36 | | - | 0.12 | 0.43 | 2.8 | 0.07 | 1.30 | 1.95 |
| $K_2O$ | 0.13 | 0.37 | 0.2 | 6.41 | 0.23 | 0.48 | 0.73 | 13.88 | 0.44 | 1.37 |
| $P_2O_5$ | 0.51 | | - | 0.19 | 0.14 | - | - | 0.26 | 0.56 | 27.93 |
| NiO | - | 0.62 | - | - | - | 0.88 | 0.85 | - | - | 0.75 |
| CoO | - | 0.41 | - | - | - | 0.85 | 0.83 | - | - | 0.78 |
| $Cr_2O_3$ | - | 0.66 | - | - | - | 0.72 | 0.37 | - | - | 0.64 |
| $V_2O_5$ | - | - | 1.0 | - | - | - | - | - | - | 0.86 |
| CuO | - | - | - | - | - | - | - | - | - | 0.74 |
| ZnO | - | - | - | - | - | - | - | - | - | 0.81 |

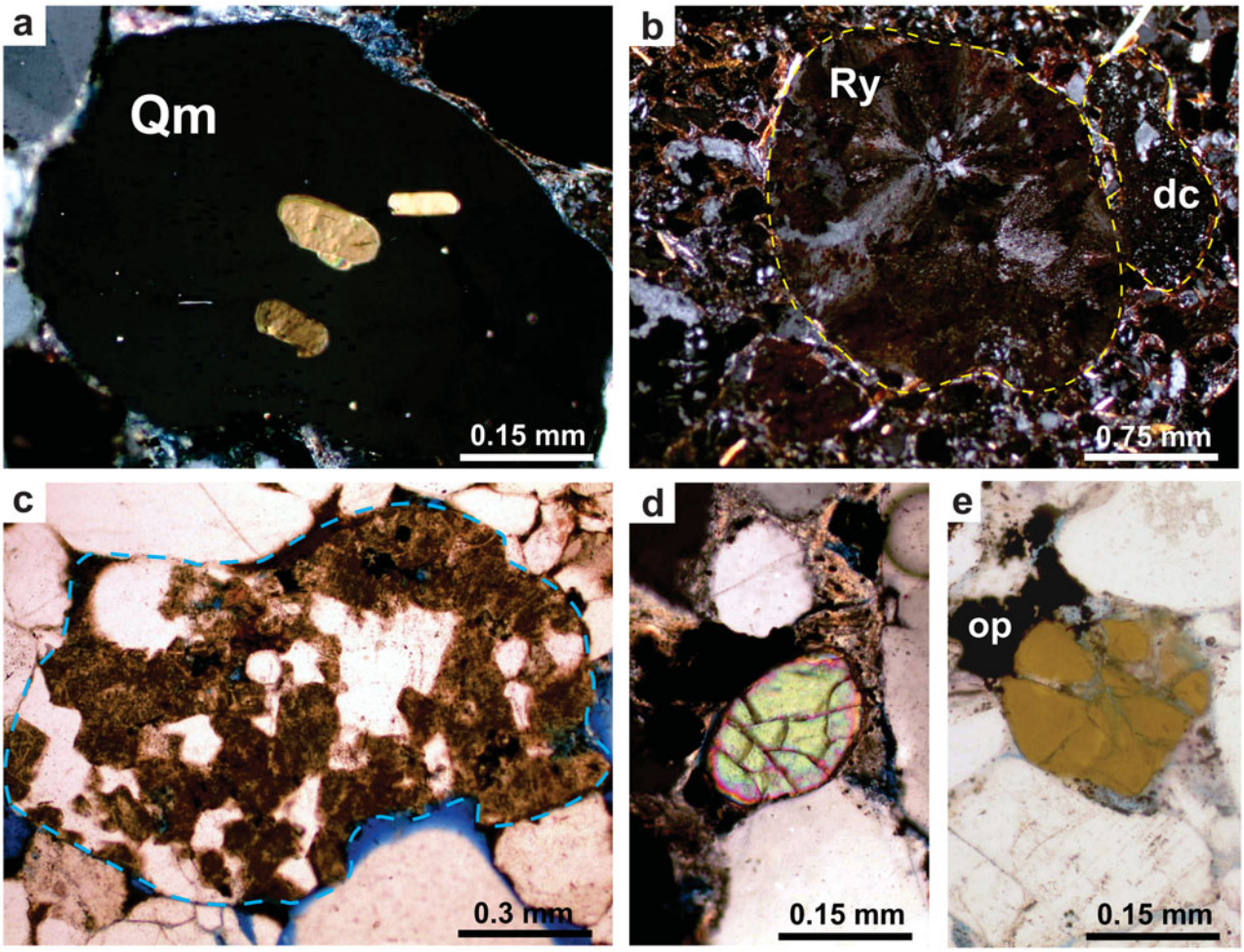


Figure 5. (Colour online) Photomicrographs of petrographic features of the Araba sandstones showing: (a) monocrystalline quartz grain (Qm) with abundant prismatic tourmaline inclusions, XPL; (b) rhyolite (Ry) and dacite (dc) fragments exhibiting spheriolitic and porphyritic textures, respectively, XPL; (c) a granitic rock fragment, PPL; (d) a zircon grain with abraded terminals, XPL; (e) an opaque (op) and a hornblende grain with fracture porosity, PPL.

https://doi.org/10.1017/S0016756815000771 Published online by Cambridge University Press

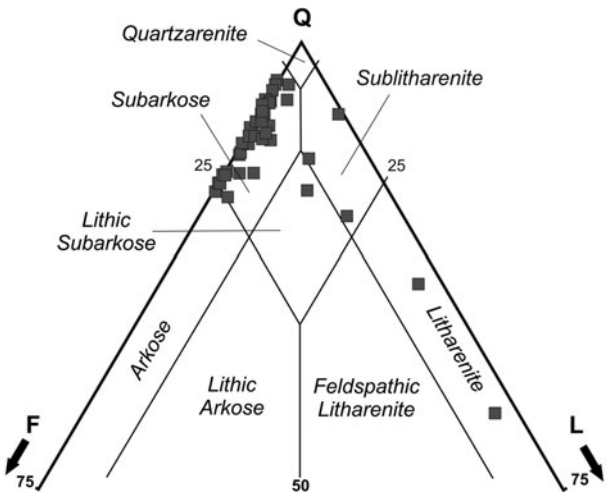


Figure 6. QFL triangle diagram showing the composition of the sandstones of the Araba Formation (after McBride, 1963). Q – quartz; F – feldspar; L – lithic grains.

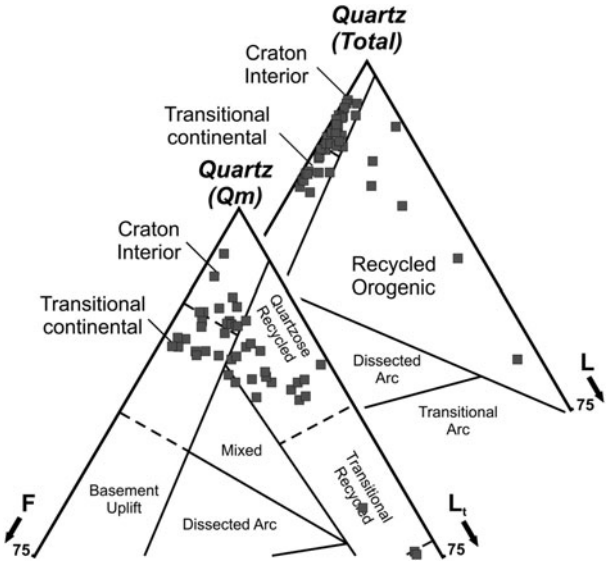


Figure 7. $Q_tFL$ and $Q_mFL_t$ ternary diagrams showing the main provenances of the Araba sandstones (after Dickinson *et al.* 1983).

It comprises only 5 % of the total clay and is characterized by 7.17, 7.16, 3.58 and 3.57Å reflections that completely collapse after being heated to 500 °C.

#### 4.c. Sandstone diagenesis

The sandstones of the Araba Formation display a variety of diagenetic features. These include mechanical infiltration of clay, compaction, precipitation of mineral cements, dissolution of detrital and diagenetic constituents, as well as grain replacement (Figs 8, 9). Most of these processes are responsible for destroying much of the primary intergranular porosity and permeability in the sandstones. Mechanical compaction is evidenced by grain packing, bending of flexible mica flakes and fracturing of quartz, feldspar and brittle rock fragments (Fig. 8a). Chemical compaction is well developed as indicated by the predominance of concave-convex and sutured grain contacts (Fig. 8b). Grain-to-grain pressure dissolution features are more well developed in clay-coat-rich sandstones than in clay-coat-poor ones.

Clay minerals are the most abundant diagenetic cements in the studied sandstones. They range in abundance from 0.8 to 27 % (av. 8.3 %; Table 1). The mixed-layer I/S has a sheet structure with lath-like, spiny projections of illite and a crinkly form of smectite (Fig. 8c). Illite occurs commonly as irregular flakes with tiny lath-like projections and fibrous pore-filling cement (Fig. 8d). Smectite occurs chiefly as a crinkly form tangentially coating detrital grains and, less commonly, as pore-filling cement plugging the intergranular porosity (Fig. 8e). Kaolinite is present as euhedral, pseudo-hexagonal plates and face-to-face vermicular stacks filling intergranular primary pores and replacing feldspars, respectively (Fig. 8f).

Iron oxides (0–24.8 %; av. 3.7 %; Table 1) occur as thin coatings around detrital grains and as scattered aggregates of pore-filling cement (Fig. 9a). Quartz cement (0–20.8 %; av. 1.2 %) mostly occurs as thick, euhedral syntaxial overgrowths around detrital quartz grains (Table 1). The overgrowth was differentiated from detrital quartz rims by fluid inclusions, thin clay and/or Fe-oxide coatings. K-Feldspar cement is present as traces (up to 0.2 %; Fig. 9b) in the form of thin, discontinuous overgrowths. Electron microprobe analyses showed virtually pure end-member $KAlSi_3O_8$ with a $K_2O$ value as high as 13.88 % and sodium concentrations of about 0.07 % (Table 2).

Calcite and dolomite are the carbonate cements (0–37 %; av. 4.6 %; Table 1) observed in the Araba sandstones. Calcite is recorded as scattered patches partially filling intergranular pores and locally filling fractures in quartz and occasionally replacing detrital quartz, feldspars and micas (Fig. 9b). Electron microprobe analyses revealed a nearly pure $CaCO_3$ end-member with minor MgO and MnO (Table 2). Dolomite occurs mainly as poikilotopic cement in the form of pore-filling, fracture-filling and, less frequently, as mosaics of tiny rhombic crystals. Occasionally, it replaces detrital quartz and feldspar grains. Dolomite crystals usually contain abundant fluid inclusions giving the crystals a turbid aspect in transmitted light. Electron microprobe analyses revealed a nearly pure $CaMgCO_3$ end-member with minor amounts of MnO (Table 2).

Barite, apatite and halite cements were detected only in a few samples (Table 1). Barite (0–2 %; av. 0.1 %), is present typically as patches of poikilotopic crystals in the form of pore-filling and fracture-filling textures with replacement features attacking the margins of surrounded framework grains such as quartz, feldspars, rock fragments and other overgrowth cements. Apatite cement (av. 0.2 %) occurs as prismatic blades up to 30 μm in length and as locally occluded pore spaces or intermixed with reddish iron-oxide materials (Fig. 9c). Electron microprobe analyses showed that apatite

https://doi.org/10.1017/S0016756815000771 Published online by Cambridge University Press

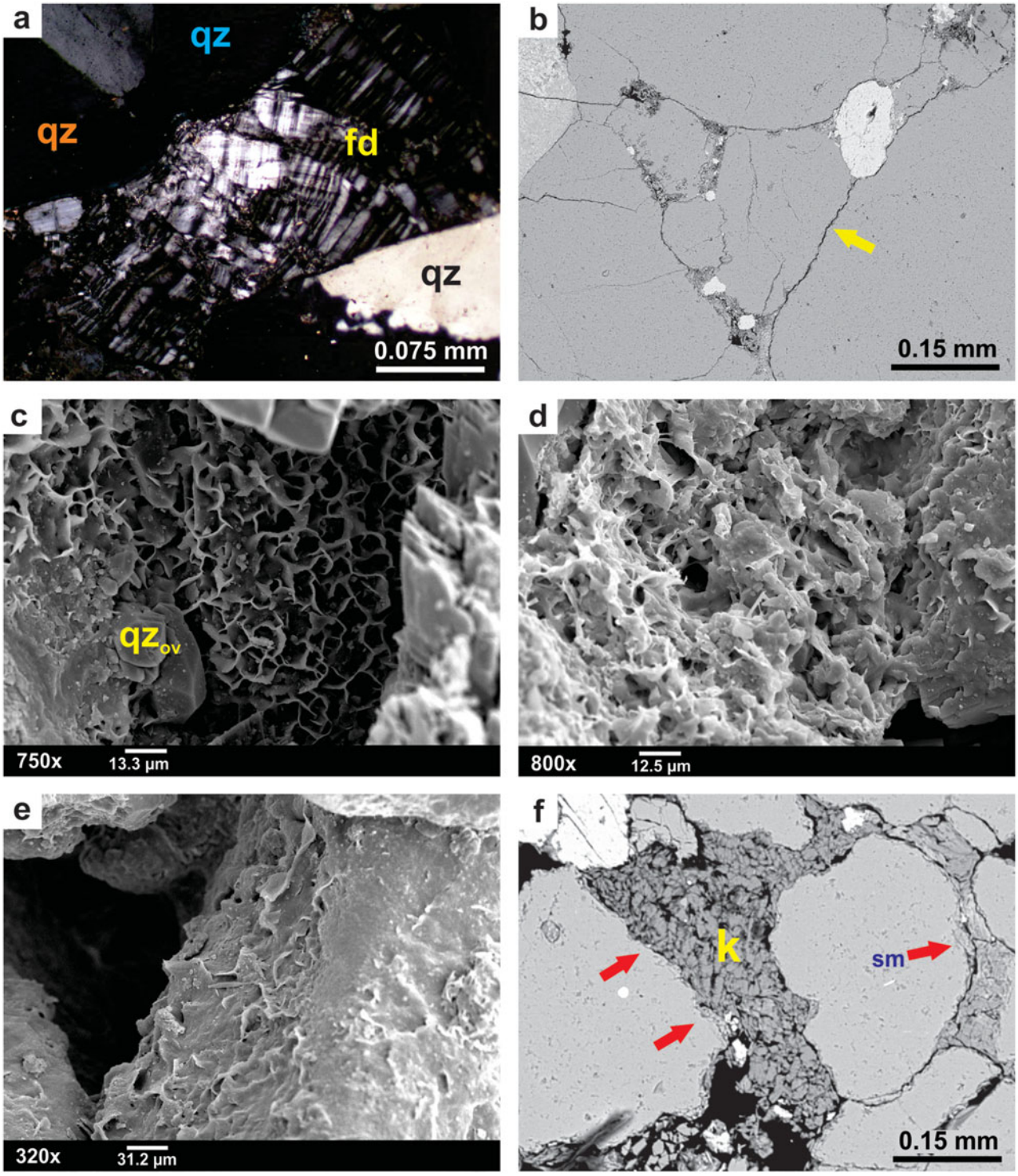


Figure 8. (Colour online) Photomicrograph, SEM and BSE images showing diagenetic features of the Araba sandstones: (a) An intensively crushed K-feldspar (fd) between rigid quartz grains (qz), XPL. (b) Sutured contact (arrow) developed along detrital quartz grains. (c) Honeycomb-shaped mixed-layer I/S clay coating engulfed by quartz overgrowth ($qz_{ov}$). (d) Fibrous illite with lath-like projections growing on I/S aggregates. (e) Tangential, cryptocrystalline smectite coating. (f) Kaolinite cement (k) completely occluding the pore spaces and engulfing smectite grain-coating (sm) (arrows).

cement is of the fluorapatite type (Table 2). Traces of halite cement lining pores is found as small cubes with rounded corners (Fig. 9d).

Unstable K-feldspar, biotite and less stable heavy minerals, as well as carbonate cements, are the phases that suffered from dissolution in these sandstones (Fig. 9e, f). Partial dissolution of mineral grains is recognized by jagged or embayed boundaries, whereas complete dissolution of detrital grains has led to the formation of mouldic macropores. Illite is observed partially or completely replacing K-feldspar grains (Fig. 9g). The replacement proceeded apparently parallel to cleavage planes. Kaolinite is observed replacing K-feldspar and muscovite forming a vermicular

https://doi.org/10.1017/S0016756815000771 Published online by Cambridge University Press

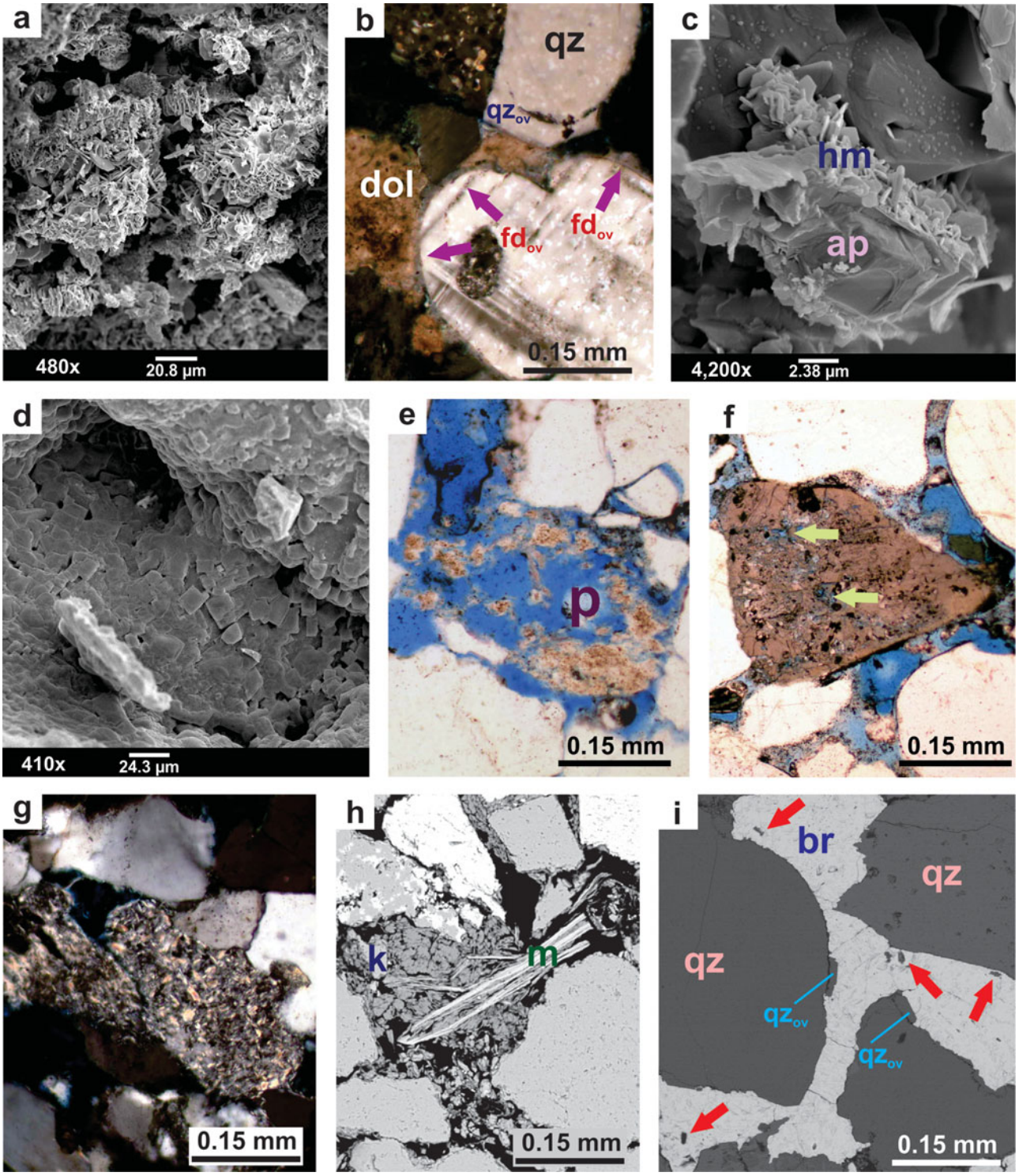


Figure 9. (Colour online) Photomicrographs, SEM and BSE images showing the diagenetic features of the Araba Formation: (a) Micro-rosettes of haematite. (b) K-feldspar overgrowth ($fd_{ov}$) replaced by late-stage poikilotopic dolomite (dol), XPL. (c) Fluorapatite blade (ap) associated with hexagonal crystals of haematite (hm). (d) Halite cement engulfing all other minerals. (e, f) Intragranular macropores (p and arrows), in K-feldspar and hornblende grains, respectively, PPL. (g) Complete illitization of feldspar grain, XPL. (h) A characteristic expanded texture of mica (m) and kaolinite (k) replacement. (i) Corrosive poikilotopic barite cement (br) invading quartz grains (qz) and their overgrowth ($qz_{ov}$). Note the floating relics (arrows).

texture and a characteristic fanning or expanded texture, respectively (Fig. 9h). Calcite, dolomite and barite are highly corrosive to detrital quartz and K-feldspar grains and their overgrowths, as marked by the presence of several projections/engulfments of these cements into grain margins (Fig. 9i).

### 4.d. Geochemistry

#### *4.d.1. Major-element geochemistry*

The sandstones of the Araba Formation have higher $SiO_2$ (av. 81.3 %), and correspondingly lower $TiO_2$ (av. 0.3 %), $Al_2O_3$ (av. 7.9 %), $Fe_2O_3$ (av. 1.5 %), MgO

https://doi.org/10.1017/S0016756815000771 Published online by Cambridge University Press

Table 3. Chemical composition of major elements (%) and trace elements (ppm) of the Araba sandstones and mudstones

| | SANDSTONE | | | | | | | | | | | | | | | | | | | |
|---|---|---|---|---|---|---|---|---|---|---|---|---|---|---|---|---|---|---|---|---|
| *Oxides (wt %)* | Tb3 | Tb5 | Tb6 | Tb8 | Tb9 | Tb10 | Tb11 | Tb12 | Tb13 | Tb14 | Tb15 | Tb16B | Tb22 | Tb24 | Tb25 | Tb31 | Tb33 | Tb34 | Tb35 | Tb36 |
| $SiO_2$ | 92.00 | 91.71 | 95.16 | 94.61 | 90.65 | 85.46 | 88.34 | 93.74 | 90.53 | 94.01 | 93.29 | 95.03 | 86.02 | 74.01 | 71.31 | 79.56 | 75.00 | 80.88 | 71.91 | 79.40 |
| $TiO_2$ | 0.25 | 0.10 | 0.10 | 0.07 | 0.45 | 0.12 | 0.09 | 0.45 | 0.10 | 0.08 | 0.16 | 0.09 | 0.17 | 0.27 | 0.28 | 0.49 | 0.45 | 0.33 | 0.72 | 0.66 |
| $Al_2O_3$ | 4.18 | 2.70 | 3.33 | 2.98 | 5.07 | 7.98 | 4.97 | 3.30 | 4.51 | 2.82 | 2.98 | 2.54 | 4.46 | 6.69 | 8.97 | 10.73 | 12.49 | 10.22 | 13.47 | 12.73 |
| $Fe_2O_3$ | 0.77 | 1.21 | 0.81 | 0.61 | 1.66 | 1.60 | 2.18 | 1.22 | 0.71 | 0.61 | 0.96 | 0.71 | 0.29 | 0.53 | 0.48 | 1.12 | 2.57 | 0.60 | 4.64 | 1.14 |
| MnO | 0.01 | 0.01 | 0.01 | 0.01 | 0.02 | 0.01 | 0.03 | 0.01 | 0.01 | 0.01 | 0.01 | 0.01 | 0.00 | 0.45 | 0.51 | 0.01 | 0.08 | 0.03 | 0.11 | 0.05 |
| MgO | 0.16 | 0.13 | 0.17 | 0.06 | 0.21 | 0.30 | 0.05 | 0.14 | 0.18 | 0.14 | 0.19 | 0.09 | 0.21 | 0.67 | 0.92 | 0.86 | 1.27 | 0.62 | 1.48 | 0.96 |
| CaO | 0.33 | 2.24 | 0.12 | 0.02 | 0.09 | 0.11 | 0.04 | 0.05 | 0.08 | 0.05 | 0.10 | 0.44 | 0.16 | 12.36 | 10.99 | 0.09 | 0.28 | 0.15 | 0.20 | 0.13 |
| $Na_2O$ | 0.15 | 0.54 | 0.85 | 0.09 | 0.17 | 0.21 | 0.08 | 0.11 | 0.13 | 0.12 | 0.10 | 0.13 | 2.56 | 0.90 | 0.36 | 0.33 | 0.38 | 0.31 | 0.37 | 0.32 |
| $K_2O$ | 2.67 | 1.68 | 2.14 | 2.00 | 3.07 | 4.31 | 3.78 | 2.06 | 2.85 | 1.76 | 1.66 | 1.65 | 2.70 | 3.31 | 5.79 | 6.02 | 6.49 | 6.24 | 6.72 | 6.62 |
| $P_2O_5$ | 0.02 | 1.57 | 0.03 | 0.02 | 0.04 | 0.03 | 0.02 | 0.17 | 0.02 | 0.02 | 0.02 | 0.08 | 0.07 | 0.08 | 0.04 | 0.04 | 0.15 | 0.09 | 0.10 | 0.08 |
| $SiO_2/Al_2O_3$ | 22 | 34 | 29 | 32 | 18 | 11 | 18 | 28 | 20 | 33 | 31 | 37 | 19 | 11 | 8 | 7 | 6 | 8 | 5 | 6 |
| $Al_2O_3/CaO + Na_2O$ | 9 | 1 | 3 | 26 | 20 | 25 | 40 | 21 | 21 | 17 | 14 | 4 | 2 | 1 | 1 | 26 | 19 | 22 | 24 | 28 |
| $K_2O/Al_2O_3$ | 18 | 3 | 3 | 21 | 18 | 21 | 46 | 19 | 21 | 15 | 16 | 13 | 1 | 4 | 16 | 19 | 17 | 20 | 18 | 21 |
| $K_2O/Na_2O$ | 18 | 3 | 3 | 21 | 18 | 21 | 46 | 19 | 21 | 15 | 16 | 13 | 1 | 4 | 16 | 19 | 17 | 20 | 18 | 21 |
| $Fe_2O_3^* + MgO$ | 1 | 1 | 1 | 1 | 2 | 2 | 2 | 1 | 1 | 1 | 1 | 1 | 0 | 1 | 1 | 2 | 4 | 1 | 6 | 2 |
| CIA | 53 | - | 46 | 56 | 57 | 60 | 54 | 57 | 57 | 56 | 58 | 48 | - | - | - | 60 | 60 | 58 | 62 | 62 |
| PIA | 60 | - | 39 | 81 | 80 | 86 | 81 | 80 | 80 | 76 | 77 | 43 | - | - | - | 86 | 83 | 81 | 86 | 88 |
| CIW | 83 | - | 67 | 94 | 92 | 94 | 96 | 93 | 93 | 91 | 89 | 72 | - | - | - | 94 | 92 | 93 | 93 | 94 |
| *Trace Elements (ppm)* | | | | | | | | | | | | | | | | | | | | |
| V | 15 | 16 | 7 | 3 | 25 | 13 | 2 | 25 | 8 | 8 | 11 | 3 | 27 | 11 | 22 | 54 | 30 | 96 | 50 | 128 |
| Cr | 13 | 13 | 7 | 6 | 14 | 11 | 125 | 23 | 8 | 8 | 14 | 8 | 14 | 14 | 11 | 21 | 26 | 15 | 35 | 28 |
| Co | 2 | 1 | 2 | 2 | 24 | 54 | 67 | 2 | 66 | 1 | 44 | 2 | 3 | 4 | 5 | 13 | 14 | 10 | 22 | 70 |
| Ni | lld | 2 | lld | lld | lld | lld | lld | lld | lld | lld | 75 | lld | 4 | 0 | 4 | 19 | 21 | 8 | 25 | 11 |
| Cu | 7 | 6 | 143 | 7 | 10 | 6 | 8 | 8 | 10 | 6 | 10 | 9 | 8 | 8 | 26 | 18 | 36 | 32 | 54 | 31 |
| Zn | 5 | 3 | 1 | 3 | 3 | 4 | 7 | 4 | lld | 1 | lld | 4 | 3 | 11 | 21 | 35 | 52 | 24 | 61 | 38 |
| Rb | 63 | 41 | 49 | 45 | 73 | 103 | 99 | 50 | 66 | 42 | 40 | 39 | 67 | 81 | 133 | 180 | 205 | 173 | 223 | 191 |
| Sr | 101 | 74 | 50 | 40 | 74 | 100 | 30 | 50 | 70 | 44 | 45 | 39 | 70 | 126 | 148 | 129 | 125 | 122 | 118 | 115 |
| Y | 9 | 10 | 6 | 10 | 16 | 6 | 39 | 7 | 4 | 5 | 10 | 11 | 19 | 21 | 15 | 12 | 19 | 13 | 29 | 21 |
| Zr | 105 | 65 | 66 | 156 | 116 | 78 | 273 | 142 | 68 | 67 | 74 | 278 | 208 | 217 | 285 | 304 | 258 | 207 | 553 | 500 |
| Nb | 8 | 6 | 5 | 6 | 12 | 5 | 15 | 11 | 5 | 5 | 6 | 6 | 10 | 8 | 9 | 14 | 13 | 10 | 18 | 17 |
| Ba | 492 | 318 | 367 | 331 | 568 | 1008 | 249 | 356 | 518 | 307 | 284 | 260 | 4847 | 663 | 931 | 849 | 843 | 992 | 850 | 892 |
| Pb | 10 | 8 | 123 | 9 | 13 | 15 | 11 | 9 | 10 | 8 | 7 | 8 | 6 | 9 | 11 | 17 | 20 | 20 | 28 | 18 |
| Th | 13 | 8 | 9 | 9 | 13 | 6 | 13 | 13 | 7 | 8 | 9 | 8 | 10 | 10 | 9 | 15 | 12 | 10 | 17 | 17 |
| Nb/Y | 1 | 1 | 1 | 1 | 1 | 1 | 0 | 2 | 1 | 1 | 1 | 1 | 1 | 0 | 1 | 1 | 1 | 1 | 1 | 1 |
| $Zr/TiO_2$ | 415 | 644 | 655 | 2393 | 259 | 654 | 2956 | 317 | 673 | 788 | 452 | 3163 | 1198 | 814 | 1030 | 618 | 578 | 628 | 763 | 753 |
| Ba/Co | 200 | 230 | 200 | 196 | 23 | 19 | 4 | 192 | 8 | 220 | 7 | 117 | 1928 | 169 | 193 | 67 | 62 | 101 | 38 | 13 |
| Th/Co | 5 | 6 | 5 | 5 | 1 | 0 | 0 | 7 | 0 | 6 | 0 | 4 | 4 | 3 | 2 | 1 | 1 | 1 | 1 | 0 |
| Cr/Th | 1 | 2 | 1 | 1 | 1 | 2 | 10 | 2 | 1 | 1 | 1 | 1 | 1 | 1 | 1 | 1 | 2 | 1 | 2 | 2 |
| Zr/Th | 8 | 9 | 8 | 17 | 9 | 14 | 22 | 11 | 9 | 8 | 8 | 35 | 20 | 21 | 31 | 21 | 21 | 21 | 33 | 29 |

Table 3. Continued

| | SANDSTONE | | | | | | | | | | | | | | | | | | | |
|---|---|---|---|---|---|---|---|---|---|---|---|---|---|---|---|---|---|---|---|---|
| *Oxides (wt %)* | Tb37 | Tb38 | Tb40A | Tb40B | Tb41 | Tb42 | Tb43A | Tb43B | Tb44 | Tb45 | Tb46 | Tb47A | Tb47B | Tb48B | Tb49 | Tb51 | Tb53 | Tb55 | Tb56 | Tb57A |
| $SiO_2$ | 87.91 | 72.23 | 72.11 | 72.79 | 67.92 | 79.43 | 69.35 | 67.81 | 78.15 | 93.31 | 88.14 | 76.06 | 77.75 | 69.09 | 82.77 | 87.50 | 86.17 | 86.92 | 74.09 | 66.30 |
| $TiO_2$ | 0.43 | 0.52 | 0.67 | 0.57 | 0.27 | 0.50 | 0.70 | 0.75 | 0.37 | 0.19 | 0.27 | 0.29 | 0.35 | 0.65 | 0.12 | 0.15 | 0.12 | 0.22 | 0.08 | 0.67 |
| $Al_2O_3$ | 3.65 | 14.11 | 11.34 | 11.31 | 7.95 | 9.56 | 14.78 | 15.49 | 11.57 | 5.26 | 5.23 | 11.47 | 11.50 | 14.56 | 7.45 | 4.53 | 7.40 | 6.59 | 3.15 | 9.49 |
| $Fe_2O_3$ | 0.36 | 3.72 | 2.14 | 2.47 | 0.08 | 0.98 | 4.69 | 5.28 | 1.43 | 0.24 | 0.26 | 1.00 | 1.01 | 3.88 | 0.59 | 0.43 | 0.41 | 0.36 | 0.43 | 2.64 |
| MnO | 0.10 | 0.06 | 0.57 | 0.48 | 1.17 | 0.07 | 0.07 | 0.09 | 0.04 | 0.00 | 0.00 | 0.01 | 0.02 | 0.04 | 0.32 | 0.00 | 0.00 | 0.01 | 1.10 | 0.01 |
| MgO | 0.18 | 1.88 | 3.46 | 3.02 | 0.89 | 0.80 | 2.01 | 2.24 | 0.80 | 0.14 | 0.19 | 1.07 | 1.05 | 1.87 | 1.44 | 0.26 | 0.38 | 0.34 | 1.80 | 1.29 |
| CaO | 2.71 | 0.19 | 3.68 | 2.95 | 12.39 | 1.43 | 0.25 | 0.32 | 0.13 | 0.07 | 1.60 | 0.18 | 0.14 | 0.10 | 1.78 | 0.15 | 0.44 | 0.26 | 16.89 | 0.29 |
| $Na_2O$ | 0.13 | 0.41 | 0.25 | 0.27 | 0.21 | 0.43 | 0.29 | 0.31 | 0.27 | 0.15 | 0.14 | 1.60 | 0.58 | 0.95 | 0.82 | 0.26 | 0.22 | 0.22 | 0.16 | 7.43 |
| $K_2O$ | 2.41 | 7.01 | 5.93 | 5.88 | 4.61 | 5.48 | 6.80 | 7.04 | 6.57 | 3.91 | 3.65 | 6.10 | 6.17 | 6.93 | 4.49 | 2.89 | 4.51 | 4.25 | 1.96 | 4.22 |
| $P_2O_5$ | 0.05 | 0.11 | 0.19 | 0.17 | 0.05 | 0.11 | 0.11 | 0.15 | 0.06 | 0.04 | 1.07 | 0.09 | 0.07 | 0.07 | 0.10 | 0.06 | 0.20 | 0.05 | 0.05 | 0.14 |
| $SiO_2/Al_2O_3$ | 24 | 5 | 6 | 6 | 9 | 8 | 5 | 4 | 7 | 18 | 17 | 7 | 7 | 5 | 11 | 19 | 12 | 13 | 24 | 7 |
| $Al_2O_3/CaO + Na_2O$ | 1 | 24 | 3 | 4 | 1 | 5 | 27 | 24 | 29 | 24 | 3 | 6 | 16 | 14 | 3 | 11 | 11 | 14 | 0 | 1 |
| $K_2O/Al_2O_3$ | 19 | 17 | 24 | 22 | 22 | 13 | 23 | 22 | 24 | 25 | 25 | 4 | 11 | 7 | 6 | 11 | 20 | 19 | 12 | 1 |
| $K_2O/Na_2O$ | 19 | 17 | 24 | 22 | 22 | 13 | 23 | 22 | 24 | 25 | 25 | 4 | 11 | 7 | 6 | 11 | 20 | 19 | 12 | 1 |
| $Fe_2O_3^* + MgO$ | 1 | 6 | 6 | 5 | 1 | 2 | 7 | 8 | 2 | 0 | 0 | 2 | 2 | 6 | 2 | 1 | 1 | 1 | 2 | 4 |
| CIA | - | 62 | - | - | - | - | 64 | 64 | 60 | 53 | - | 55 | - | 61 | - | 54 | - | 55 | - | - |
| PIA | - | 87 | - | - | - | - | 89 | 88 | 87 | 73 | - | 62 | - | 80 | - | 67 | - | 70 | - | - |
| CIW | - | 93 | - | - | - | - | 94 | 93 | 94 | 93 | - | 79 | - | 89 | - | 87 | - | 89 | - | - |
| *Trace Elements (ppm)* | | | | | | | | | | | | | | | | | | | | |
| V | 24 | 63 | 47 | 56 | 22 | 270 | 61 | 67 | 33 | 9 | 13 | 233 | 307 | 59 | 28 | 27 | 57 | 13 | 12 | 41 |
| Cr | 12 | 44 | 34 | 34 | 12 | 23 | 45 | 50 | 18 | 8 | 9 | 17 | 17 | 45 | 19 | 35 | 13 | 9 | 8 | 21 |
| Co | 4 | 20 | 29 | 13 | 8 | 12 | 21 | 19 | 8 | 3 | 2 | 20 | 8 | 13 | 23 | 60 | 4 | 64 | 14 | 5 |
| Ni | lld | 43 | 15 | 16 | 7 | 10 | 24 | 29 | 12 | 2 | 1 | 10 | 10 | 20 | 1 | 3 | 4 | lld | lld | 8 |
| Cu | 30 | 39 | 42 | 43 | 24 | 60 | 36 | 45 | 22 | 11 | 10 | 21 | 27 | 23 | 10 | 9 | 14 | 9 | 28 | 7 |
| Zn | 3 | 71 | 64 | 64 | 15 | 38 | 87 | 99 | 27 | 4 | 5 | 16 | 32 | 71 | 15 | 3 | 9 | 6 | 18 | 7 |
| Rb | 55 | 241 | 179 | 179 | 113 | 152 | 218 | 228 | 181 | 101 | 98 | 170 | 172 | 229 | 116 | 71 | 117 | 113 | 49 | 112 |
| Sr | 88 | 117 | 116 | 109 | 173 | 106 | 109 | 108 | 117 | 65 | 78 | 171 | 160 | 97 | 76 | 109 | 123 | 114 | 134 | 109 |
| Y | 13 | 77 | 39 | 33 | 31 | 22 | 22 | 26 | 12 | 11 | 16 | 10 | 11 | 17 | 14 | 6 | 13 | 7 | 26 | 18 |
| Zr | 490 | 107 | 598 | 432 | 239 | 498 | 403 | 408 | 286 | 256 | 376 | 192 | 270 | 298 | 100 | 81 | 80 | 187 | 190 | 611 |
| Nb | 11 | 8 | 16 | 14 | 7 | 13 | 16 | 17 | 11 | 10 | 10 | 9 | 10 | 15 | 7 | 6 | 5 | 8 | 4 | 15 |
| Ba | 6098 | 956 | 744 | 722 | 1055 | 855 | 803 | 746 | 1020 | 514 | 508 | 1455 | 1647 | 857 | 2674 | 6502 | 1054 | 730 | 1107 | 738 |
| Pb | 9 | 21 | 18 | 17 | 14 | 17 | 26 | 26 | 20 | 10 | 13 | 16 | 17 | 20 | 9 | 10 | 16 | 15 | 14 | 12 |
| Th | 12 | 6 | 18 | 16 | 8 | 16 | 15 | 18 | 11 | 11 | 15 | 9 | 9 | 15 | 12 | 5 | 6 | 9 | 7 | 19 |
| Nb/Y | 1 | 0 | 0 | 0 | 0 | 1 | 1 | 1 | 1 | 1 | 0.6 | 0.9 | 0.9 | 0.9 | 0.5 | 1.0 | 0.4 | 1.1 | 0.2 | 0.8 |
| $Zr/TiO_2$ | 1145 | 209 | 890 | 759 | 886 | 995 | 574 | 546 | 769 | 1338 | 1398 | 658 | 768 | 457 | 835 | 537 | 686 | 830 | 2465 | 906 |
| Ba/Co | 1680 | 47 | 26 | 55 | 128 | 73 | 38 | 40 | 125 | 183 | 327 | 72 | 205 | 67 | 116 | 109 | 279 | 11 | 78 | 139 |
| Th/Co | 3 | 0 | 1 | 1 | 1 | 1 | 1 | 1 | 1 | 4 | 10 | 0 | 1 | 1 | 1 | 0 | 2 | 0 | 0 | 4 |
| Cr/Th | 1 | 7 | 2 | 2 | 2 | 1 | 3 | 3 | 2 | 1 | 1 | 2 | 2 | 3 | 2 | 7 | 2 | 1 | 1 | 1 |
| Zr/Th | 42 | 17 | 34 | 28 | 29 | 30 | 27 | 23 | 27 | 23 | 25 | 22 | 31 | 20 | 9 | 16 | 13 | 22 | 27 | 32 |

Table 3. Continued

| | SANDSTONE | | | | | | | MUDSTONE | | | | | | | | | | |
|---|---|---|---|---|---|---|---|---|---|---|---|---|---|---|---|---|---|---|
| *Oxides (wt %)* | Tb57B | Tb58 | Tb59 | Tb60 | Tb61 | Av. | UCC | Tb17 | Tb23 | Tb29 | Tb30B | Tb32B | Tb39B | Tb50B | Tb52B | Tb54B | Av. | PAAS |
| $SiO_2$ | 74.03 | 51.70 | 78.04 | 89.27 | 89.11 | 81.3 | 66.00 | 63.41 | 55.78 | 59.45 | 58.16 | 61.91 | 62.74 | 61.06 | 59.48 | 53.07 | 59.4 | 62.80 |
| $TiO_2$ | 0.53 | 0.29 | 0.40 | 0.09 | 0.09 | 0.3 | 0.50 | 0.77 | 0.77 | 1.10 | 1.16 | 0.89 | 0.79 | 0.86 | 0.82 | 0.63 | 0.9 | 1.00 |
| $Al_2O_3$ | 11.28 | 7.70 | 11.06 | 6.55 | 6.05 | 7.9 | 15.20 | 16.96 | 19.15 | 20.83 | 22.27 | 18.13 | 16.71 | 18.29 | 18.50 | 15.31 | 18.5 | 18.90 |
| $Fe_2O_3$ | 4.12 | 2.56 | 1.47 | 0.25 | 0.31 | 1.5 | 5.00 | 6.01 | 6.44 | 6.65 | 5.59 | 8.63 | 7.02 | 7.04 | 7.14 | 6.20 | 6.7 | 6.30 |
| MnO | 0.02 | 0.01 | 0.01 | lld | 0.01 | 0.1 | 0.08 | 0.09 | 0.16 | 0.07 | 0.05 | 0.11 | 0.28 | 0.05 | 0.05 | 0.04 | 0.1 | 0.11 |
| MgO | 1.27 | 1.46 | 1.03 | 0.27 | 0.25 | 0.8 | 2.02 | 2.93 | 3.04 | 3.20 | 3.11 | 2.43 | 3.53 | 3.03 | 3.22 | 2.63 | 3.0 | 2.20 |
| CaO | 0.54 | 0.23 | 0.39 | 0.24 | 0.09 | 1.7 | 4.20 | 0.81 | 1.17 | 0.21 | 0.22 | 0.25 | 1.48 | 0.71 | 0.30 | 0.27 | 0.6 | 1.30 |
| $Na_2O$ | 0.57 | 13.37 | 0.26 | 0.25 | 0.47 | 0.8 | 3.90 | 0.43 | 4.63 | 0.59 | 0.56 | 0.35 | 0.39 | 0.97 | 1.95 | 9.93 | 2.2 | 1.20 |
| $K_2O$ | 5.96 | 3.25 | 5.94 | 3.92 | 3.86 | 4.4 | 3.40 | 7.64 | 6.88 | 7.48 | 7.63 | 7.01 | 7.34 | 7.07 | 6.89 | 4.74 | 7.0 | 3.70 |
| $P_2O_5$ | 0.13 | 0.09 | 0.08 | 0.02 | 0.02 | 0.1 | NA | 0.15 | 0.15 | 0.04 | 0.05 | 0.08 | 0.18 | 0.16 | 0.13 | 0.13 | 0.1 | 0.16 |
| $SiO_2/Al_2O_3$ | 7 | 7 | 7 | 14 | 15 | 14 | - | 4 | 3 | 3 | 3 | 3 | 4 | 3 | 3 | 3 | 3 | - |
| $Al_2O_3/CaO + Na_2O$ | 10 | 1 | 17 | 13 | 11 | 13 | - | 14 | 3 | 26 | 29 | 30 | 9 | 11 | 8 | 2 | 15 | - |
| $K_2O/Al_2O_3$ | 10 | 0 | 23 | 16 | 8 | 16 | - | 18 | 1 | 13 | 14 | 20 | 19 | 7 | 4 | 0 | 11 | - |
| $K_2O/Na_2O$ | 10 | 0 | 23 | 16 | 8 | 16 | - | 18 | 1 | 13 | 14 | 20 | 19 | 7 | 4 | 0 | 11 | - |
| $Fe_2O_3^* + MgO$ | 5 | 4 | 2 | 1 | 1 | 2 | - | 9 | 9 | 10 | 9 | 11 | 11 | 10 | 10 | 9 | 10 | - |
| CIA | 57 | - | 59 | 56 | 54 | 57 | - | - | - | - | - | - | - | - | - | - | - | - |
| PIA | 71 | - | 80 | 73 | 67 | 76 | - | - | - | - | - | - | - | - | - | - | - | - |
| CIW | 85 | - | 91 | 89 | 87 | 89 | - | - | - | - | - | - | - | - | - | - | - | - |
| *Trace Elements (ppm)* | | | | | | | | | | | | | | | | | | |
| V | 44 | 22 | 34 | 4 | 5 | 47 | 60 | 64 | 72 | 100 | 111 | 84 | 77 | 104 | 110 | 69 | 88 | 150 |
| Cr | 24 | 16 | 16 | 7 | 8 | 21 | 35 | 54 | 76 | 91 | 91 | 72 | 58 | 85 | 85 | 60 | 75 | 110 |
| Co | 22 | 4 | 18 | 19 | 4 | 18 | 10 | 26 | 29 | 33 | 43 | 27 | 26 | 21 | 17 | 29 | 28 | 23 |
| Ni | 10 | 3 | 8 | lld | lld | 14 | 20 | 49 | 45 | 55 | 42 | 44 | 33 | 35 | 29 | 32 | 40 | 55 |
| Cu | 11 | 8 | 8 | 13 | 14 | 22 | 25 | 465 | 66 | 82 | 74 | 55 | 63 | 20 | 17 | 8 | 95 | 50 |
| Zn | 35 | 6 | 34 | 6 | 13 | 24 | 71 | 111 | 82 | 164 | 182 | 121 | 125 | 121 | 95 | 30 | 114 | 85 |
| Rb | 184 | 86 | 173 | 104 | 108 | 122 | 112 | 268 | 236 | 394 | 374 | 303 | 258 | 262 | 258 | 154 | 278 | 160 |
| Sr | 149 | 91 | 139 | 125 | 107 | 101 | 350 | 175 | 144 | 144 | 150 | 144 | 101 | 125 | 92 | 99 | 131 | 200 |
| Y | 14 | 8 | 13 | 5 | 3 | 17 | 22 | 25 | 18 | 18 | 22 | 37 | 27 | 24 | 24 | 25 | 25 | 27 |
| Zr | 294 | 202 | 344 | 83 | 77 | 247 | 190 | 282 | 177 | 227 | 236 | 250 | 255 | 206 | 209 | 140 | 220 | 210 |
| Nb | 12 | 8 | 10 | 6 | 6 | 10 | 25 | 18 | 17 | 25 | 26 | 18 | 16 | 17 | 17 | 12 | 18 | 19 |
| Ba | 900 | 528 | 954 | 722 | 671 | 1122 | 550 | 782 | 654 | 747 | 580 | 740 | 677 | 677 | 567 | 522 | 660 | 650 |
| Pb | 21 | 9 | 18 | 15 | 13 | 17 | 20 | 20 | 312 | 24 | 17 | 30 | 28 | 23 | 22 | 6 | 54 | 20 |
| Th | 10 | 10 | 13 | 7 | 7 | 11 | 11 | 17 | 19 | 18 | 24 | 16 | 16 | 17 | 18 | 16 | 18 | 15 |
| Nb/Y | 0.9 | 1.0 | 0.8 | 1.1 | 1.6 | 1 | - | 0.7 | 0.9 | 1.4 | 1.2 | 0.5 | 0.6 | 0.7 | 0.7 | 0.5 | 1 | - |
| $Zr/TiO_2$ | 559 | 703 | 857 | 886 | 879 | 918 | - | 367 | 231 | 206 | 203 | 282 | 325 | 240 | 256 | 223 | 259 | - |
| Ba/Co | 40 | 148 | 54 | 38 | 177 | 183 | - | 31 | 23 | 23 | 14 | 27 | 26 | 33 | 33 | 18 | 25 | - |
| Th/Co | 0 | 3 | 1 | 0 | 2 | 2 | - | 1 | 1 | 1 | 1 | 1 | 1 | 1 | 1 | 1 | 1 | - |
| Cr/Th | 2 | 2 | 1 | 1 | 1 | 2 | - | 3 | 4 | 5 | 4 | 5 | 4 | 5 | 5 | 4 | 4 | - |
| Zr/Th | 30 | 20 | 26 | 11 | 11 | 21 | - | 17 | 9 | 12 | 10 | 16 | 16 | 12 | 11 | 9 | 13 | - |

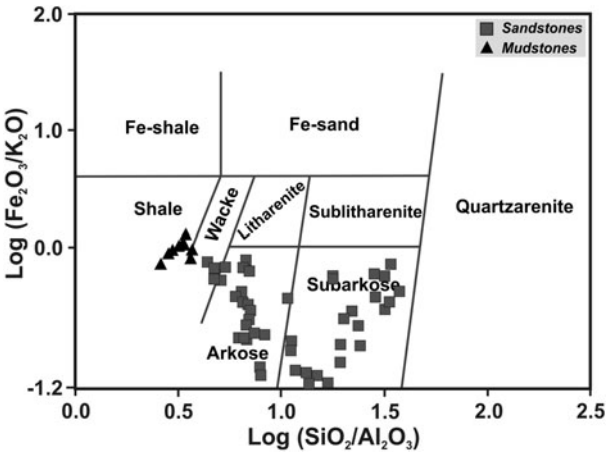


Figure 10. Geochemical classification of the sandstones and mudstones of the Araba Formation (after Herron, 1988).

(av. 0.8 %) and $K_2O$ (av. 4.4 %) contents than in the mudstones (Table 3). Based on the chemical classification diagram of Herron (1988), the sandstones are mostly classified as arkoses to subarkoses and the mudstones as shales (Fig. 10).

The relationships between $SiO_2$ and $TiO_2$ ($r = -0.62$; $n = 45$), $Al_2O_3$ ($r = -0.73$; $n = 45$), $Fe_2O_3$ ($r = -0.58$; $n = 45$), MgO ($r = -0.76$; $n = 45$) and $K_2O$ ($r = -0.64$; $n = 45$) for the sandstones of the Araba Formation are statistically not significant. However, in the mudstones, this correlations are slightly different ($r = 0.30$, $-0.00$, 0.39, 0.25 and 0.75; $n = 9$, respectively). Similarly, in the sandstones, the correlations between $Al_2O_3$ and $TiO_2$ ($r = 0.80$; $n = 45$), $Fe_2O_3$ ($r = 0.70$; $n = 45$), MgO ($r = 0.72$; $n = 45$) and $K_2O$ ($r = 0.97$; $n = 45$) are statistically significant (Fig. 11b), whereas, in the mudstones, except for $TiO_2$ and $K_2O$ ($r = 0.92$ and 0.60, respectively; $n = 9$), the correlations are statistically not significant for $Fe_2O_3$ and MgO ($r = -0.21$ and 0.26, respectively; $n = 9$). On the other hand, both MnO and $Fe_2O_3{}^* + MgO$ are positively correlated with MgO ($r = 0.65$; $n = 54$) and $Al_2O_3$ ($r = 0.89$; $n = 54$), respectively.

Generally, the sandstone and mudstone samples from the Araba Formation have $K_2O/Na_2O$ values $>>1$ (av. 16 and 11, respectively; Table 3). On average, the Araba sandstones are slightly enriched in $SiO_2$ and MnO, as well as in $K_2O$ contents and depleted in other elements compared to the upper continental crust (UCC; Taylor & McLennan, 1985; Fig. 11a). On the other hand, the mudstones show a mostly similar composition to the Post Archaean Australian Shale (PAAS; Taylor & McLennan, 1985), except for MgO, $K_2O$, $Na_2O$ and CaO (Fig. 11b).

#### *4.d.2. Trace-element geochemistry*

The trace-element concentrations and elemental ratios are presented in Table 3. The trace-element concentrations in the clastic sediments of the Araba Formation are normalized to the average UCC and PAAS values

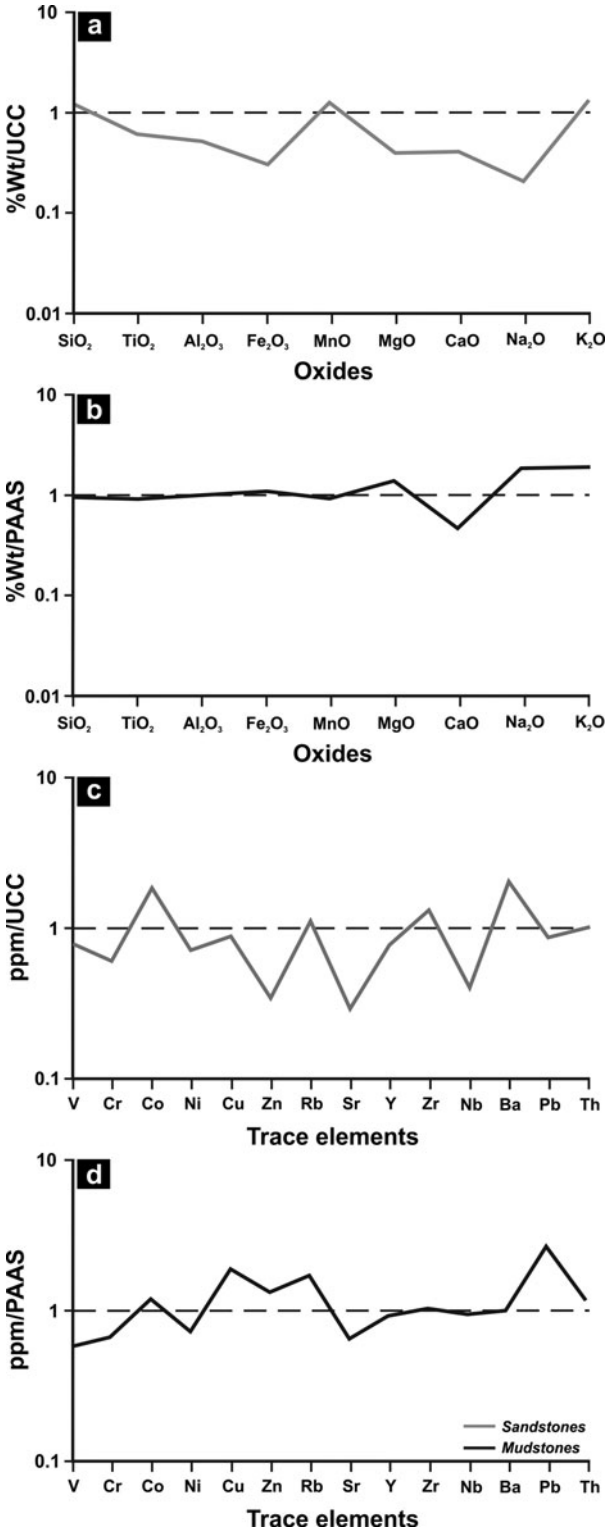


Figure 11. Multi-element plots of average chemistry of the Araba Formation normalized against UCC and PAAS (Taylor & McLennan, 1985). (a) Major-element concentrations of sandstones normalized against UCC; (b) major-element concentrations of mudstones normalized against PAAS; (c) trace-element concentrations of sandstones normalized against UCC; and (d) trace-element concentrations of mudstones normalized against PAAS.

https://doi.org/10.1017/S0016756815000771 Published online by Cambridge University Press

(Fig. 11c, d, respectively). The abundances of large ion lithophile elements (LILEs), such as Rb, Ba and Sr, are similar in the sandstone and mudstone samples but are different relative to the UCC and PAAS. In the sandstone and mudstone samples, Rb and Ba are enriched but Sr is depleted relative to the UCC and PAAS (Fig. 11c, d, respectively). Rb, Ba and Sr contents are positively correlated with both $Al_2O_3$ (r = 0.97, 0.61 and 0.40, respectively; n = 54) and $K_2O$ (r = 0.93, 0.68 and 0.54, respectively; n = 54).

The concentrations of high-field-strength elements (HFSEs) such as Y, Zr, Nb and Th are similar in the sandstone and mudstone samples but show different behaviour to the UCC and PAAS (Fig. 11c, d, respectively). The average concentration of Zr is relatively enriched in the sandstones and mudstones (av. 247 and 220 ppm, respectively), while Th is enriched only in the mudstones (av. 18 ppm). In contrast, Y (av. 17 and 25 ppm) and Nb (av. 10 and 18 ppm) are depleted in the sandstone and mudstone samples. Meanwhile, the HFSEs (Y, Zr, Nb and Th) for the sandstones and mudstones are positively correlated with $TiO_2$ (r = 0.44, 0.47, 0.93 and 0.86, respectively; n = 54). On the other hand, Nb and Th are positively correlated with $Al_2O_3$ (r = 0.83 and 0.71, respectively; n = 54) and $K_2O$ (r = 0.75 and 0.59, respectively; n = 54). The average Zr content for the sandstones is higher than in the mudstones.

The transition trace elements (TTEs) including V, Cr, Co, Ni and Zn in the sandstones and mudstones show different abundances relative to the UCC and PAAS (Fig. 11c, d, respectively). In comparison with the UCC and PAAS, the V, Cr and Ni contents are lower and Co content is higher in the sandstone and mudstone samples, respectively (Fig. 11c, d). The Zn content is higher in the mudstone than in the sandstone samples, as well as compared to the average PAAS value (Fig. 11c, d; Table 3). The TTEs, V, Cr, Ni and Zn in the sandstone and mudstone samples are positively correlated with $TiO_2$ (r = 0.41, 0.70, 0.70 and 0.89, respectively; n = 54), $Al_2O_3$ (r = 0.49, 0.72, 0.71 and 0.91, respectively; n = 54), $Fe_2O_3$ (r = 0.25, 0.80, 0.74 and 0.85, respectively; n = 54) and $K_2O$ (r = 0.53, 0.57, 0.57 and 0.80, respectively; n = 54). In contrast, Co has shown no significant correlation with other elements. The Th/Co and Cr/Th ratios in the sandstones and mudstones vary from 0.1 to 9.5 and 0.6 to 9.9, respectively (Table 3).

## 5. Discussion

### 5.a. Mineral authigenesis

The grain-to-grain pressure dissolution features are well pronounced in the clay-coated and mica-rich sandstones of the Araba Formation indicating that intergranular clays played a major role in quartz dissolution. This dissolution is enhanced along mica contacts as a consequence of local pH increase arising from the interaction of mica surfaces with the adjoining pore fluids (Oelkers, Bjørkum & Murphy, 1992).

The important factors that favour smectite formation in the Araba sandstones are mostly attributed to (1) the low-lying topography and poor drainage, which may have led to favourable chemical conditions for the formation of smectite (Aoudjit *et al.* 1995); and (2) semi-arid climatic conditions during weathering with minimal throughput of water and limited ability to lose cations (e.g. $Ca^{2+}$, $Mg^{2+}$, $Na^{+}$ and $K^{+}$). In weathered granitic rocks of the French Armorican Massif, poorly drained and relatively stagnant groundwater conditions in a downslope position (with the water enriched in silica and basic cations) have led to the preferential formation of dioctahedral smectite (montmorillonite; Aoudjit *et al.* 1995). The local dissolution of detrital framework grains can result in smectite growth at the expense of plagioclase and glassy volcanic grains in plagioclase-rich arkoses and litharenites (Ryu & Niem, 1999).

At increasing burial depth, smectite was likely to be converted into illite via mixed-layer I/S. This conversion was controlled by a combination of burial depth, temperature, time and also percentage of K-feldspar in the succession. Illite is probably formed during burial by the degradation of smectite at temperatures around 100 °C (Chuhan, Bjørlykke & Lowery, 2000). On the other hand, kaolinite is probably derived from K-feldspars and micas which acted as a likely source of Al and Si (De Ros, 1998).

The iron incorporated in the haematite cement was likely released by the breakdown of unstable Fe-bearing minerals (e.g. pyroxene, amphibole and biotite; Schöner & Gaupp, 2005). These labile mafic minerals are partly prone to diagenetic alteration and suggest that the pigmentation process took place during the earlier stage of diagenesis.

Silica needed for quartz overgrowth is probably derived from the dissolution of K-feldspar; illitization of eodiagenetic smectite during burial; transformation of kaolinite into illite; and pressure dissolution (Madhavaraju *et al.* 2002). Quartz cement is inhibited by grain-coating clays, which is normally attributed to a reduction in the surface area available for nucleation of authigenic quartz. Al and Si participating in K-feldspar cement were probably internally sourced by the alteration of detrital silicates, particularly feldspars. However, other sources of silica, such as pressure solution or illitization of smectitic clays, cannot be excluded.

The presence of poikilotopic calcite cement filling large intergranular pores in loosely packed sandstones with a floating grain texture, as well as its occurrence filling fractures in quartz or replacing detrital grains, probably indicates two stages of formation. Calcium needed for eodiagenetic calcite is derived from the dissolution of unstable grains such as plagioclase, hornblende and volcanic rock fragments (Moraes & De Ros, 1990). Conversely, calcium incorporated in mesodiagenetic calcite is linked to the illitization of smectite in the sandstones and interstratified mudstones.

https://doi.org/10.1017/S0016756815000771 Published online by Cambridge University Press

The potential contributors of magnesium in the Araba sandstones are believed to be the dissolution of biotite and the conversion of smectite to illite during diagenesis. This conversion is a common diagenetic process which is capable of releasing large amounts of Fe, Mg, Ca, Na and Si. Smectite–illite conversion is invoked as the source of ions necessary for late-stage dolomites.

The sulfate involved in barite formation and the presence of halite cement in these sandstones may be sourced from the overlying Lower Cretaceous Malha Formation and/or possibly from seawater. Such a source of sulfate has been demonstrated elsewhere in deeply buried sandstones from different basins (e.g. Sullivan *et al.* 1994). A plausible internal source of $Ba^{2+}$ is the dissolution of K-feldspar. This is consistent with the common association of K-feldspar and barite cements in the Araba sandstones.

The occurrence of apatite cement in the Araba sandstones is probably related to recrystallization of detrital apatite which was derived from acidic igneous rocks (Weissbrod & Nachmias, 1987). However, phosphorous may be contributed from the nearby weathered basement, since continental weathering is likely the most important source of phosphorous. Thus, the combination of Ca, F and $PO_4$ under basic conditions may have led to the precipitation of fluorapatite cement. Apatite cement has been previously recorded in Lower Palaeozoic sandstones of SW Sinai (Kordi, Turner & Salem, 2011) and neighbouring countries (e.g. Israel, southern Jordan and NW Arabia; Weissbrod & Nachmias, 1987).

### 5.b. Geochemical composition

The petrological and geochemical classifications of the Araba sandstones show a similar behaviour. The plotting of sandstone samples within the arkosic field (Fig. 10) is attributed to the presence of aluminous clay minerals. The enrichment of silica in the sandstones relative to the mudstones together with their negative correlations with $TiO_2$, $Al_2O_3$, $Fe_2O_3$, MgO and $K_2O$, confirms that most of the silica is incorporated in quartz grains. The differences in correlation coefficient values between the sandstones and mudstones are probably attributed to dilution by quartz (Cullers, 2000). Similarly, the higher contents of $Al_2O_3$, $TiO_2$, $Fe_2O_3$ and $K_2O$ in the mudstone samples reflect their association with clay-sized phases. In general, $Al_2O_3$ and trace-element concentrations increase as grain size and $SiO_2$ content decrease (Armstrong-Altrin *et al.* 2012, 2013). The common association of $TiO_2$, $Fe_2O_3$, MgO, $Fe_2O_3 + MgO^*$ and $K_2O$ in the mudstones indicates that these elements are absorbed onto clay minerals and metal oxides (Das, Al-Mikhlafi & Kaur, 2006). The elevated $K_2O/Na_2O$ ratios in the Araba sandstones and mudstones are attributed to the higher proportion of K-bearing minerals such as K-feldspar, muscovite and illite compared to Na-plagioclases (Table 1).

The depletion of the major-element concentrations in the Araba sandstones, compared to the UCC, is not only attributed to quartz dilution but also indicates that chemical weathering has led to the removal of soluble elements from the clastic fraction compared to insoluble hydrolysates. The slightly elevated MnO content in the sandstones is possibly due to Mn mineralization, which is consistent with the Cu–Mn mineralization recorded in the Cambrian Timna Formation of Israel (A. Segev, unpub. Ph.D. thesis, Hebrew Univ. Jerusalem, Jerusalem, 1986). However, electron microprobe analysis of dolomite (sample Tb 28; Table 2) and the close association of MnO with MgO (Table 3) may support a diagenetic origin.

$K_2O$ is slightly enriched as a result of K-metasomatism during illite formation. According to Fedo, Nesbitt & Young (1995), K-metasomatism of sandstones can take two different paths, representing (1) conversion of aluminous clay minerals to illite, and/or (2) conversion of plagioclase to K-feldspar. K-metasomatism was also documented from the Lower Cambrian sediments of Israel (Sandler, Teutsch & Avigad, 2012). The lower CaO and $Na_2O$ contents in the sandstones together with a lack of elemental relationships suggest the destruction of plagioclases during chemical weathering in the source area and/or during sediment transport. On the other hand, the notable enrichment of MgO, $K_2O$ and $Na_2O$ in the mudstones is possibly linked to phyllosilicates, K-metasomatism and halite cement, respectively.

The enrichment of Rb in the sandstones and mudstones is related to the common occurrence of detrital K-feldspar, whereas Ba enrichment in the sandstones is attributed to the presence of diagenetic barite cement. However, the lower content of Sr is probably due to the deficiency of calcic plagioclase. The close association of Rb, Sr and Ba with $Al_2O_3$ and $K_2O$ suggests that their distribution is mainly controlled by phyllosilicate minerals (Etemad-Saeed, Hosseini-Barzi & Armstrong-Altrin, 2011). The enrichment of Zr content is generally due to the occurrence of zircon minerals (Armstrong-Altrin *et al.* 2013). The elevated content of Zr in the sandstones compared to the mudstones is due to preferential concentration of zircons in the coarse-grained sands, unlike Nb, which is usually absorbed onto clay minerals in mudstones. The moderately positive correlation between Y and Zr against $TiO_2$ suggests that their behaviour is mainly controlled by detrital heavy minerals. In contrast, significant correlations between Nb and Th v. $TiO_2$, $Al_2O_3$ and $K_2O$ imply their association in clay minerals and/or other Ti- and Nb-bearing phases (Etemad-Saeed *et al.* 2015).

The depletion or enrichment of V, Co, Cr and Ni in clastic sediments provides a significant clue to the source rock (Cullers, 2000). A positive correlation between V, Cr, Ni and Zn versus $TiO_2$, $Al_2O_3$ and $Fe_2O_3$ indicates their intimate relationship to Fe–Ti oxides, as well as clay minerals. The high value of Co in the Araba sediments may suggest some input of mafic materials from the source area (Armstrong-Altrin *et al.*

https://doi.org/10.1017/S0016756815000771 Published online by Cambridge University Press

2004). Nevertheless, simultaneous depletion of other TTEs like Cr, Ni and V indicates that the enrichment of Co in the sandstones is probably linked to copper mineralization (A. Segev, unpub. Ph.D. thesis, Hebrew Univ. Jerusalem, Jerusalem, 1986).

### 5.c. Provenance

The combination of petrographic and geochemical data is an important tool to determine the provenance of clastic sediments. The high proportion of angular monocrystalline quartz together with rounded polycrystalline grains in the Araba sandstones indicates that they were derived from various sources with different transport distances. The dominance of unstrained monocrystalline grains over strained ones points to a plutonic origin. The observed inclusions of bipyramidal zircon and prismatic microlites of tourmaline within quartz grains indicate derivation from volcanic, plutonic or metamorphic rocks (Blatt, Middleton & Murray, 1980; Loi & Dabard, 1997). Meanwhile, the occurrence of embayed and euhedral monocrystalline grains reflects a silicic volcanic origin (Blatt, Middleton & Murray, 1980).

The presence of a wide variety of polycrystalline grains including curved, sutured and crenulated intercrystalline boundaries with variable numbers of subcrystals and a wide spectrum of crystal shapes indicates derivation from composite/mixed sources. The polycrystalline quartz grains with two to five subcrystals and straight to slightly curved intercrystalline boundaries suggest a plutonic source (Blatt, Middleton & Murray, 1980), whereas those with five or more elongated crystals with sutured and crenulated intercrystalline subcrystal boundaries indicate a metamorphic terrain (Asiedu *et al.* 2000). The predominance of K-feldspar over plagioclase together with muscovite and biotite micas suggests a plutonic source (Osae *et al.* 2006). The common existence of the ultrastable zircon–tourmaline–rutile (ZTR) group with minor amounts of hornblende and apatite grains suggests their derivation from igneous source rocks (Asiedu *et al.* 2000).

Using major oxides as variables, Roser & Korsch (1988) established a discriminant function diagram to differentiate four major provenance fields: mafic, intermediate, felsic and quartzose recycled. Figure 12 shows that most of the sandstones and mudstones of the Araba Formation are plotted in the recycled sedimentary field, suggesting their derivation from a cratonic interior or recycled origin. Unlike major oxides, certain trace elements such as LILEs, HFSEs and some TTEs are mostly useful in the determination of provenance, as they have relatively low mobility during sedimentary processes and short residence times in seawater (Bhatia, 1983; Cullers, 2000). Plotting the data on the Cr/V–Y/Ni (Hiscott, 1984) and $TiO_2$–Ni diagrams (Floyd *et al.* 1991; Figs 13, 14) reveals that the sandstones and mudstones were mostly derived from felsic source rocks. Furthermore, the ratios of Th/Co and Cr/Th in the sediments of the Araba Formation are

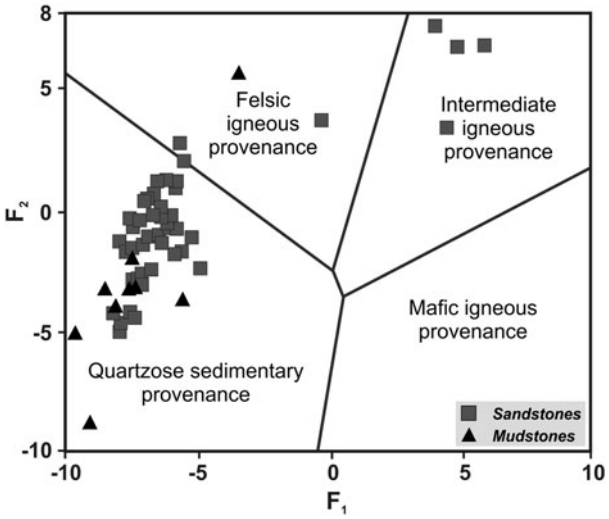


Figure 12. Provenance discriminant function plot for the Araba sandstones and mudstones (after Roser & Korsch, 1988).

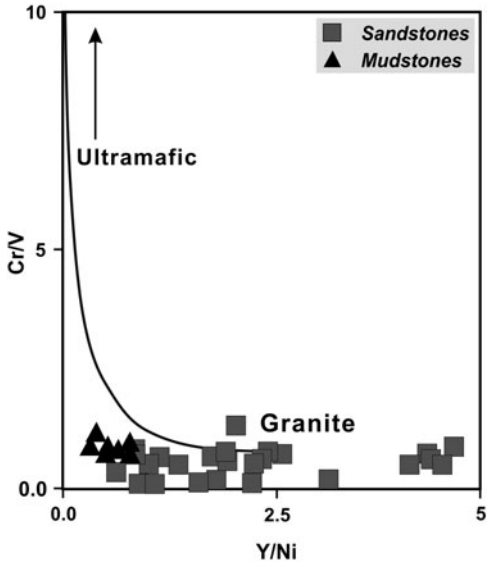


Figure 13. Cr/V v. Y/Ni diagram for the Araba sandstones and mudstones (after Hiscott, 1984).

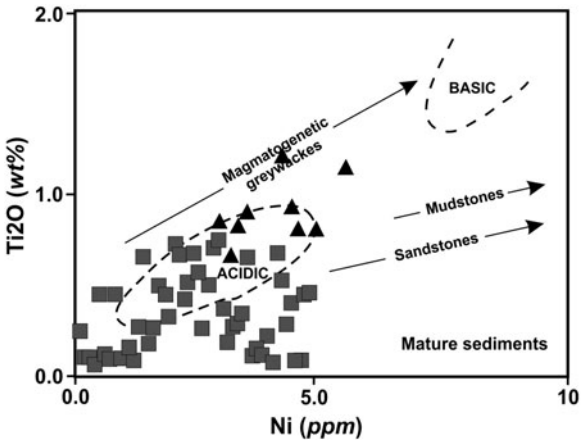


Figure 14. $TiO_2$–Ni diagram for the Araba sandstones and mudstones (after Floyd *et al.* 1991).

https://doi.org/10.1017/S0016756815000771 Published online by Cambridge University Press

also consistent with those derived from felsic source rocks (Cullers, 2000).

Field-based indications for the sense of transport suggest that the quartz-rich sand was conveyed from the Gondwana hinterland towards the open ocean in the north (Fig. 4). Such northward transportation to the northern margin of Gondwana has previously been recorded from the Cambrian sediments of North Africa, the Sinai Peninsula and Arabia (Avigad *et al.* 2012).

### 5.d. Tectonic setting

The modal data of the Araba sandstones mostly plot in the craton interior field (Fig. 7), comprising high quartzose detritus with less than 10 % feldspars, and nearly all of them are potassic. These sandstones were derived from relatively low-lying granitoid and gneissic terrain that was supplemented by recycled sands from associated platform or passive margin basins (Dickinson *et al.* 1983). However, samples plotted within the recycled orogenic field indicate that the sediment sources are dominantly sedimentary with subordinate volcanic rocks derived from tectonic settings where stratified rocks are deformed, uplifted and eroded (Dickinson & Suczek, 1979).

Various diagrams are available to identify the tectonic setting of a source region (e.g. Bhatia, 1983; Roser & Korsch, 1986) and are continuously used in many studies. These diagrams were evaluated by other researchers and they cautioned against the use of these previously proposed discrimination diagrams (e.g. Armstrong-Altrin & Verma 2005; Ryan & Williams, 2007). Recently, Verma & Armstrong-Altrin (2013) proposed two new discriminant-function-based major-element diagrams for the tectonic discrimination of siliciclastic sediments from three main tectonic settings; island or continental arc, continental rift and collision have been created for the tectonic discrimination of high-silica ($(SiO_2)adj = 63-95\,\%$) and low-silica rocks ($(SiO_2)adj = 35-63\,\%$). These diagrams were used in recent studies to discriminate the tectonic setting of a source region, based on sediment geochemistry (Armstrong-Altrin *et al.* 2014; Zaid & Gahtani, 2015; Armstrong-Altrin, 2015; Armstrong-Altrin *et al.* 2015). According to these high- and low-silica diagrams (Fig. 15a, b), most of the Araba sediments are plotted within the collision field.

The ANS is by far the largest tract of mostly juvenile Neoproterozoic crust among the regions of Africa that were affected by the Pan-African orogenic cycle. This crust was sandwiched between continental tracts of East and West Gondwana. The precise timing of the collision is still being resolved, but appears to have occurred after ~ 630 Ma but before ~ 610 Ma (Kröner & Stern, 2004). The terminal collision between East and West Gondwana may have continued for a few tens of millions of years. Compared to the southern ANS, deformation in the northern ANS part was considerably less affected by the collision that ended by the beginning of Cambrian time. Accordingly, the N–W-trending left-lateral faults of the Najd Fault System of Arabia and Egypt were formed as a result of escape tectonics associated with the collision.

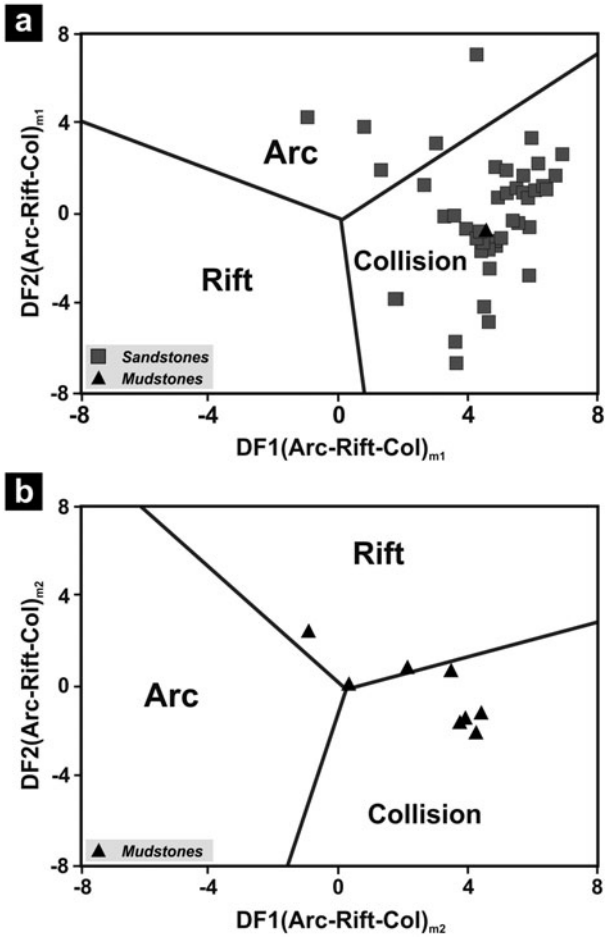


Figure 15. New discriminant function multidimensional diagrams for (a) high-silica and (b) low-silica clastic sediments of the Araba Formation (after Verma & Armstrong-Altrin, 2013). The subscripts $_{m1}$ and $_{m2}$ in DF1 and DF2 are based on $\log_{e-}$ and log ratios of major elements. The discriminant function equations are: $DF1(Arc–Rift–Col)_{m1} = (-0.263 \times \ln(TiO_2/SiO_2)_{adj}) + (0.604 \times \ln(Al_2O_3/SiO_2)_{adj}) + (-1.725 \times \ln(Fe_2O_3{}^t/SiO_2)_{adj}) + (0.660 \times \ln(MnO/SiO_2)_{adj}) + (2.191 \times \ln(MgO/SiO_2)_{adj}) + (0.144 \times \ln(CaO/SiO_2)_{adj}) + (-1.304 \times \ln(Na_2O/SiO_2)_{adj}) + (0.054 \times \ln(K_2O/SiO_2)_{adj}) + (-0.330 \times \ln(P_2O_5/SiO_2)_{adj}) + 1.588$. $DF2(Arc–Rift–Col)_{m2} = (-1.196 \times \ln(TiO_2/SiO_2)_{adj}) + (1.604 \times \ln(Al2O_3/SiO_2)_{adj}) + (0.303 \times \ln(Fe_2O_3{}^t/SiO_2)_{adj}) + (0.436 \times \ln(MnO/SiO_2)_{adj}) + (0.838 \times \ln(MgO/SiO_2)_{adj}) + (-0.407 \times \ln(CaO/SiO_2)_{adj}) + (1.021 \times \ln(Na_2O/SiO_2)_{adj}) + (-1.706 \times \ln(K_2O/SiO_2)_{adj}) + (-0.126 \times \ln(P_2O_5/SiO_2)_{adj}) - 1.068$.

### 5.e. Palaeo-weathering and climate

The most widely used chemical indices to assess the degree of chemical weathering in the source area are the CIA (Nesbitt & Young, 1982), CIW (Harnois, 1988) and PIA (Fedo, Nesbitt & Young, 1995). Chemical weathering increases under humid conditions, with leaching of cations (e.g. $Na^+$, $K^+$ and $Ca^{2+}$) and the concentration of Al and Si in the residue. Conversely, in an environment dominated by physical weathering,

https://doi.org/10.1017/S0016756815000771 Published online by Cambridge University Press

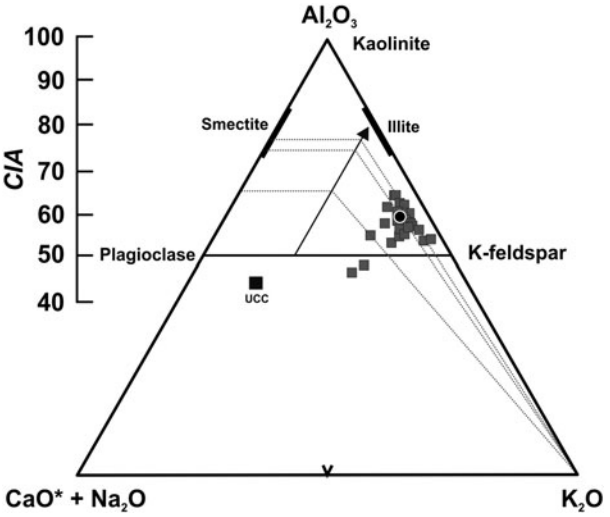


Figure 16. $Al_2O_3$–$CaO^* + Na_2O$–$K_2O$ ternary diagram for the Araba sandstones (after Nesbitt & Young, 1984). Arrow refers to trend of initial weathering profile of granite.

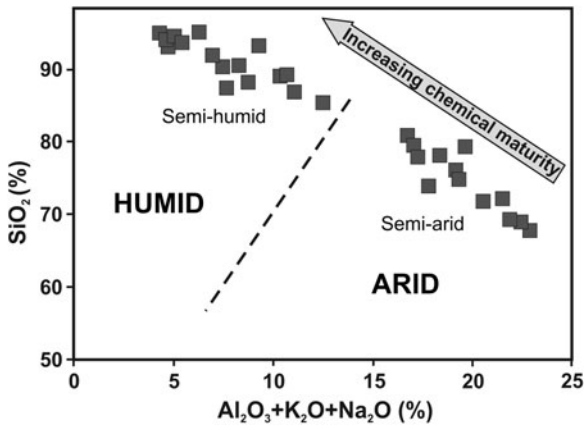


Figure 17. Chemical maturity of the Araba sandstones (after Suttner & Dutta, 1986).

abrasion is the primary producer of sediments by mechanical breakdown into smaller grain sizes. The chemical alteration of feldspars to form clay minerals is thus negligible under physical weathering.

The CIA is a good measure of palaeo-weathering conditions, and it essentially monitors the progressive weathering of feldspars to clay minerals (Fedo, Nesbitt & Young, 1995; Armstrong-Altrin *et al.* 2004). The systematic progression in alteration of minerals is incipient (CIA = 50–60) to intermediate (CIA = 60–80) to extreme (CIA > 80) chemical weathering. Excluding samples rich in carbonate, halite and apatite cements, the calculated values of the CIA vary from 46 to 64 (av. 57; Table 3). These values suggest that the Araba sandstones were subjected to incipient chemical weathering at the source area (Nesbitt & Young, 1982).

In the A–CN–K diagram (Nesbitt & Young, 1984), the samples of the Araba sandstones typically plot in a trend following the A–K join and close to the K-apex (Fig. 16). The deviation from the predicted weathering trend is probably attributable to differential dissolution of labile minerals, as plagioclases are more easily dissolved than K-feldspar. This is confirmed by the petrographic study and indicated by elevated $K_2O/Na_2O$ ratios (Table 3). This deviation could also be related to a metasomatic increase in K during diagenesis, caused by the conversion of aluminous clay minerals to illite (Fedo, Nesbitt & Young, 1995). Accordingly, the studied Araba sandstones exhibit a lower CIA than the original values. Several authors have emphasized the importance of $K^+$ correction (e.g. Price & Velbel, 2003). Based on the predicted weathering trend of granite, the reconstructed CIA values range from 65 to 77 (av. 74) implying moderate chemical weathering (Fig. 16).

Although a precise CIA value cannot be ascertained, the alternative CIW index is used in this study to monitor palaeo-weathering at the source area. Harnois (1988) proposed the CIW index, which is not sensitive to post-depositional K enrichments. The siliciclastic sediments of the Araba Formation possess CIW values ranging from ~ 67 to 96 (av. 89). These high values probably suggest a prolonged dissolution of unstable plagioclases during transportation and/or diagenesis, other than extreme chemical weathering at the source terrain.

The degree of chemical weathering can also be evaluated using the PIA (Fedo, Nesbitt & Young, 1995). The studied sandstones have a wide range of PIA values (39–89; av. 76) indicating that a great deal of plagioclases have been converted into clay minerals. This, in turn, is consistent with the data obtained using the CIA, and indicates moderate weathering at the source area. The presence of K-feldspar, the common presence of biotite mica and the scarcity of hornblende and apatite are also in harmony with the weathering indices of the Araba sandstones.

Climate affects sand composition through its destructive influence on parent rocks. In this study, the palaeoclimatic condition prevailing during Cambrian time over north Gondwanaland was inferred from the bi-plots of Suttner & Dutta (1986). This diagram seems to be a sensitive discriminator of sandstones with different climate heritage. The major-element concentrations demonstrate the significance of both humid and arid climatic conditions (Fig. 17). The presence of smectite clay coating, especially in the lower and middle parts of the succession, supports an arid to semi-arid climate. In addition, the occurrence of evaporates and ventifacts in the Cambrian of north Gondwana indicates residence under a warm to arid climate (Álvaro *et al.* 2000). On the other hand, Knox, Soliman & Essa (2011) argued that the stratigraphic variation in ATi (apatite–tourmaline index) values within the Cambrian sandstones of Sinai is the result of variation in climate or the rate of erosion and transport. This result is in harmony with the data obtained by Avigad *et al.* (2005) and Tawfik *et al.* (2011) who attributed the Cambro-Ordovician siliciclastic sediments to intensive chemical weathering of the Pan-African continental basement in a warm-humid climate that prevailed

https://doi.org/10.1017/S0016756815000771 Published online by Cambridge University Press

over north Gondwana from the end of Neoproterozoic time to pre-glacial Ordovician time, hence, indicating that the environmental conditions may have fluctuated considerably.

## 6. Conclusions

Integrated petrographic and geochemical studies of the Cambrian Araba Formation exposed in east Sinai, Egypt, provided important information on the diagenetic overprints, provenance, tectonic setting, intensity of weathering and climate signature prevailing in north Gondwana during that time. The formation consists dominantly of sandstone with mudstone and rarely conglomerate interbeds and was deposited in fluvio-marine environments.

Unlike other mature Cambrian quartzarenites of Yeman, Saudi Arabia, southwestern Egypt and the Egyptian Eastern Desert, the studied sandstones possess a sub-mature, subarkosic composition. They also show some variation in lithic and heavy mineral compositions, indicating a relatively short transport distance and different proximal source areas. Diagenetic features that affected these sandstones are: mechanical infiltration of smectite and kaolinite; physical and chemical compactions; cementation by clays, iron oxides, quartz, feldspar, calcite, dolomite, barite, apatite and halite; dissolution; and clay replacement.

The recorded N–NW palaeocurrent directions in the fluvio-conglomeratic layer together with its rock fragment composition indicate their derivation from the neighbouring Precambrian terrains. Modal composition and geochemical indices (Cr/V, Y/Ni, Th/Co and Cr/Th ratios) of the sandstones and mudstones suggest their derivation from felsic source rocks on the northern fringe of the ANS.

Usage of the modern tectonic discrimination plots has revealed that the Araba succession had been originally deposited in a collisional setting. Such a setting is consistent with the collision that occurred between East and West Gondwana that most likely followed the closure of the Mozambique Ocean, forming the East African Orogen.

Palaeo-weathering indices such as the CIA, CIW and PIA suggest that the source area was moderately chemically weathered. This conclusion suggests that earlier subarkosic Cambrian sands were derived from local erosion of moderately weathered basement rocks on the northern fringe of the ANS, probably under fluctuating climatic conditions.

**Acknowledgements.** This work was fully supported by the Japanese Ministry of Education, Culture, Sports, Science and Technology, MONBUKAGAKUSHO (H.A.T., grant number 072534); and the International Association of Sedimentologists, IAS (H.A.T., postgraduate grant scheme 2010, 2nd session). J.S.A. is grateful to the Instituto de Ciencias del Mar y Limnología, UNAM Institutional project (no. 616). The authors are greatly indebted to Dr Takeshi Kuritani, Hokkaido University, for facilitating the use of laboratory equipment and Prof. Luiz F. De Ros, Universidade Federal do Rio Grande do Sul, for the comments on the earlier version of the manuscript. Editor P. Leat and two anonymous reviewers are thanked for their constructive comments.

## References

Álvaro, J. M., Rouchy, J. M., Beschstadt, T., Boucot, A., Boyer, F., Debrenee, F., Moreno-Eiris, E., Perejón, A. & Venin, E. 2000. Evaporitic constraints on the southward drifting of western Gondwana margins during Early Cambrian times. *Palaeogeography, Palaeoclimatology, Palaeoecology* **160**, 105–22.

Aoudjit, H., Robert, M., Elsass, F. & Curmi, P. 1995. Detailed study of smectite genesis in granitic saprolites by analytical electron microscopy. *Clay Mineralogy* **30**, 135–47.

Armstrong-Altrin, J. S. 2015. Evaluation of two multidimensional discrimination diagrams from beach and deep-sea sediments from the Gulf of Mexico and their application to Precambrian clastic sedimentary rocks. *International Geology Review* **57**, 1446–61.

Armstrong-Altrin, J. S., Lee, Y. I., Kasper-Zubillagaa, J. J., Carranza-Edwards, A., Garcia, D., Eby, G. N., Balaram, V. & Cruz-Ortiz, N. L. 2012. Geochemistry of beach sands along the western Gulf of Mexico, Mexico: implication for provenance. *Chemie der Erde* **72**, 345–62.

Armstrong-Altrin, J. S., Lee, Y. I., Verma, S. P. & Ramasamy, S. 2004. Geochemistry of sandstones from the upper Miocene Kudankulam Formation, Southern India: implications for provenance, weathering, and tectonic setting. *Journal of Sedimentary Research* **74**, 285–97.

Armstrong-Altrin, J. S., Machain-Castillo, M. L., Rosales-Hoz, L., Carranza-Edwards, A., Sanchez-Cabeza, J. A. & Ruíz-Fernández, A. C. 2015. Provenance and depositional history of continental slope sediments in the Southwestern Gulf of Mexico unraveled by geochemical analysis. *Continental Shelf Research* **95**, 15–26.

Armstrong-Altrin, J. S., Nagarajan, R., Lee, Y. I., Kasper-Zubillaga, J. J. & Córdoba-Saldaña, L. P. 2014. Geochemistry of sands along the San Nicolás and San Carlos beaches, Gulf of California, Mexico: implications for provenance and tectonic setting. *Turkish Journal of Earth Sciences* **23**, 533–58.

Armstrong-Altrin, J. S., Nagarajan, R., Madhavaraju, J., Rosales-Hoz, L., Lee, Y. I., Balaram, V., Cruz-Martinez, A. & Avila-Ramirez, G. 2013. Geochemistry of the Jurassic and upper Cretaceous shales from the Molango Region, Hidalgo, Eastern Mexico: implications for source-area weathering, provenance, and tectonic setting. *Comptes Rendus Geosciences* **345**,185–202.

Armstrong-Altrin, J. S. & Verma, S. P. 2005. Critical evaluation of six tectonic setting discrimination diagrams using geochemical data of Neogene sediments from known tectonic settings. *Sedimentary Geology* **177**, 115–29.

Asiedu, D. K., Suzuki, S., Nogami, K. & Shibata, T. 2000. Geochemistry of Lower Cretaceous sediments, Inner Zone of Southwest Japan: constraints on provenance and tectonic environment. *Geochemical Journal* **34**, 155–73.

Avigad, D., Gerdes, A., Morag, N. & Bechstädt, T. 2012. Coupled U–Pb–Hf of detrital zircons of Cambrian sandstones from Morocco and Sardinia: implications for

provenance and Precambrian crustal evolution of North Africa. *Gondwana Research* **21**, 690–703.

AVIGAD, D., SANDLER, A., KOLODNER, K., STERN, R. J., MCWILLIAMS, M., MILLER, N. & BEYTH, M. 2005. Mass-production of Cambro-Ordovician quartz-rich sandstone as a consequence of chemical weathering of Pan-African terranes: environmental implications. *Earth and Planetary Science Letters* **240**, 818–26.

BELLINI, E. & MASSA, D. 1980. A stratigraphic contribution to the Paleozoic of the southern basins of Libya. In *The Geology of Libya* (eds M. Salem & M. Busrevil), pp. 3–56. London: Academic Press.

BHATIA, M. R. 1983. Plate tectonics and geochemical composition of sandstones. *Journal of Geology* **91**, 611–27.

BLATT, H., MIDDLETON, G. & MURRAY, R. 1980. *Origin of Sedimentary Rocks*. Prentice-Hall, 768 pp.

CAO, J., WU, M., CHEN, Y., HU, K., BIAN, L., WANG, L. & ZHANG, Y. 2012. Trace and rare earth element geochemistry of Jurassic mudstones in the northern Qaidam Basin, northwest China. *Chemie der Erde* **72**, 245–52.

CHUHAN, F. A., BJØRLYKKE, K. & LOWERY, C. 2000. The role of provenance in illitization of deeply buried reservoir sandstones from Haltenbanken and North Viking Graben, offshore Norway. *Marine and Petroleum Geology* **17**, 673–89.

CULLERS, R. L. 2000. The geochemistry of shales, siltstones and sandstones of Pennsylvanian-Permian age, Colorado, USA: implications for provenance and metamorphic studies. *Lithosphere* **51**, 181–203.

DAS, B. K., AL-MIKHLAFI, A. S. & KAUR, P. 2006. Geochemistry of Mansar lake sediments, Jammu, India: implication for source-area weathering, provenance, and tectonic setting. *Journal of Asian Earth Sciences* **26**, 649–68.

DE ROS, L. F. 1998. Heterogeneous generation and evolution of diagenetic quartzarenites in the Silurian–Devonian Fumas Formation of the Paran Basin, southern Brazil. *Sedimentary Geology* **116**, 99–128.

DICKINSON, W. R., BEARD, L. S., BRAKENRIDGE, G. R., ERJAVEC, J. L., FERGUSON, R. C., INMAN, K. F., KNEPP, R. A., LINDBERG, F. A. & RYBERG, P. T. 1983. Provenance of North American Phanerozoic sandstones in relation to tectonic setting. *Geological Society of America Bulletin* **94**, 222–35.

DICKINSON, W. R. & SUCZEK, C. A. 1979. Plate tectonics and sandstone compositions. *American Association of Petroleum Geologists Bulletin* **63**, 2164–82.

EL SHAHAT, A. & KORA, M. 1986. Petrology of the Early Paleozoic rocks of Um Bogma area, Sinai. *Mansoura Science Bulletin* **13**, 151–84.

ETEMAD-SAEED, N., HOSSEINI-BARZI, M. & ARMSTRONG-ALTRIN, J. S. 2011. Petrography and geochemistry of clastic sedimentary rocks as evidences for provenance of the Lower Cambrian Lalun Formation, Posht-e-badam block, Central Iran. *Journal of African Earth Sciences* **61**, 142–59.

ETEMAD-SAEED, N., HOSSEINI-BARZI, M., EDABI, M. H., SADEGHI, A. & HOUSHMANDZADEH, A. 2015. Provenance of Neoproterozoic sedimentary basement of northern Iran, Kahar Formation. *Journal of African Earth Sciences* **111**, 54–75.

FEDO, C. M., NESBITT, H. W. & YOUNG, G. M. 1995. Unraveling the effects of potassium metasomatism in sedimentary rocks and paleosols, with implications for paleoweathering conditions and provenance. *Geology* **23**, 921–4.

FLOYD, P. A., SHAIL, R., LEVERIDGE, B. E. & FRANKE, W. 1991. Geochemistry and provenance of Rhenohercynian synorogenic sandstones: implications for tectonic environment discrimination. In *Developments in Sedimentary Provenance Studies* (eds A. C. Morton, S. P. Todd & P. D. W. Haughton), pp. 173–88. Geological Society of London, Special Publication no. 57.

GHANDOUR, I. M., TAWFIK, H. A., MAEJIMA, W. & ABDEL-HAMEED, A. T. 2013. Sedimentary facies and sequence stratigraphy of the Cambrian Araba Formation, Gebel Somr El-Qaa'a, North Wadi Qena, Egypt. *Neues Jahrbuch für Geologie und Paläontologie* **268**, 149–74.

GHIENNE, J.-F., BOUMENDJEL, K., PARIS, F., VIDET, B., RACHEBOEUF, P. & SALEM, H. A. 2007. The Cambrian–Ordovician succession in the Ougarta Range (western Algeria, North Africa) and interference of the Late Ordovician glaciations on the development of the Lower Paleozoic transgression on northern Gondwana. *Bulletin of Geosciences* **82**, 183–214.

HARNOIS, L. 1988. The CIW index: a new chemical index of weathering. *Sedimentary Geology* **55**, 319–22.

HERRON, M. M. 1988. Geochemical classification of terrigenous sands and shales from core or log data. *Journal of Sedimentary Petrology* **58**, 820–9.

HISCOTT, R. N. 1984. Provenance of deep-water sandstones, Tourelle Formation, Quebec, and implications for the initiation of the Taconic orogeny. *Canadian Journal of Earth Sciences* **15**, 1579–97.

ISSAWI, B. & JUX, U. 1982. Contributions to the stratigraphy of the Palaeozoic rocks in Egypt. *Geological Survey of Egypt* **64**, 28.

JOHNSON, P. R., ANDRESEN, A., COLLINS, A. S., FOWLER, A. R., FRITZ, H., GHEBREAB, W., KUSKY, T. & STERN, R. J. 2011. Late Cryogenian–Ediacaran history of the Arabian-Nubian Shield: a review of depositional, plutonic, structural, and tectonic events in the closing stages of the northern East African Orogen. *Journal of African Earth Sciences* **61**, 167–232.

KEELEY, M. L. 1989. The Paleozoic history of the Western Desert of Egypt. *Basin Research* **2**, 35–48.

KNOX, R. W. O.'B., SOLIMAN, M. F. & ESSA, M. A. 2011. Heavy mineral stratigraphy of Palaeozoic and Mesozoic sandstones of southwestern Sinai, Egypt: a reassessment. *GeoArabia* **16**, 31–64.

KORDI, M., TURNER, B. & SALEM, A. M. 2011. Linking diagenesis to sequence stratigraphy in fluvial and shallow marine sandstones: evidence from the Cambrian–Ordovician lower sandstone unit in southwestern Sinai, Egypt. *Marine and Petroleum Geology* **28**, 1554–71.

KRÖNER, A. & STERN, R. J. 2004. Pan-African orogeny. *Encyclopedia of Geology* **1**, 1–12.

LLOYD, J., 1968. The hydrogeology of the southern desert of Jordan. In *Sandstone Aquifer of Jordan*, pp. 53. U.N.D.P. Mission Report.

LOI, A. & DABARD, M. P. 1997. Zircon typology and geochemistry in the paleogeographic reconstruction of the Late Ordovician of Sardinia (Italy). *Journal of Sedimentary Geology* **112**, 263–79.

MADHAVARAJU, J., RAMASAMY, S., RUFFELL, A. & MOHAN, S. P. 2002. Clay mineralogy of the Late Cretaceous and early Tertiary successions of the Cauvery Basin (southeastern India): implications for sediment source and palaeoclimates at the K/T boundary. *Cretaceous Research* **23**, 153–63.

MCBRIDE, E. F. 1963. Classification of common sandstones. *Journal of Sedimentary Petrology* **33**, 664–9.

MCBRIDE, E. F. 1977. Secondary porosity – importance in sandstone reservoirs in Texas. *Gulf Coast Association of Geological Societies Transactions* **27**, 121–2.

MOGHAZI, A. M. 2003. Geochemistry and petrogenesis of a high-K calcalkaline Dokhan volcanic suite. South Safaga area, Egypt: the role of late Neoproterozoic crustal extension.*Precambrian Research* **125**, 116–78.

MORAES, M. A. S. & DE ROS, L. F. 1990. Infiltrated clays in fluvial Jurassic sandstones of Reconcavo basin, Northeastern Brazil. *Journal of Sedimentary Petrology* **6**, 809–19.

NESBITT, H. W. & YOUNG, G. M. 1984. Prediction of some weathering trends of plutonic and volcanic rocks based on thermodynamic and kinetic considerations. *Geochimica et Cosmochimica Acta* **48**, 1523–34.

NESBITT, H. W. & YOUNG, G. M. 1982. Early Proterozoic climates and plate motions inferred from major element chemistry of lutites. *Nature* **299**, 715–7.

OELKERS, E. H., BJØRKUM, P. A. & MURPHY, W. M. 1992. The mechanism of porosity reduction, stylolite development and quartz cementation in North Sea sandstones. In *Water–Rock Interaction* (eds Y. K. Kharaka & A. S. Maest), pp. 1183–86. Rotterdam: Balkema.

OMARA, S. 1972. An Early Cambrian outcrop in southwestern Sinai, Egypt. *Neues Jahrbuch für Geologie und Paläontologie* **5**, 306–14.

OSAE, S., ASIEDU, D. K., BANOENG-YAKUBO, B., KOEBERL, C. & DAMPARE, S. B. 2006. Provenance and tectonic setting of Late Proterozoic Buem sandstones of southeastern Ghana: evidence from geochemistry and detrital modes. *Journal of African Earth Sciences* **44**, 85–96.

POWELL, C. MC. A., PREISS, W. V., GATEHOUSE, C. G., KRAPEZ, B. & LI, Z. X. 1994. South Australian record of a Rodinian epicontinental basin and its mid-Neoproterozoic breakup to form the Palaeo-Pacific Ocean. *Tectonophysics* **237**, 113–40.

PRICE, J. R. & VELBEL, M. A. 2003. Chemical weathering indices applied to weathering profiles developed on heterogeneous felsic metamorphic parent rocks. *Chemical Geology* **202**, 397–416.

ROSER, B. P. & KORSCH, R. J. 1986. Determination of tectonic setting of sandstone-mudstone suites using $SiO_2$ content and $K_2O/Na_2O$ ratio. *Journal of Geology* **94**, 635–50.

ROSER, B. P. & KORSCH, R. J. 1988. Provenance signature of sandstone-mudstone suite determined using discriminant function analysis of major element data. *Chemical Geology* **67**, 119–39.

RYAN, K. M. & WILLIAMS, D. M. 2007. Testing the reliability of discrimination diagrams for determining the tectonic depositional environment of ancient sedimentary basins. *Chemical Geology* **242**, 103–25.

RYU, I. & NIEM, A. R. 1999. Sandstone diagenesis, reservoir potential, and sequence stratigraphy of the Eocene Tyee basin, Oregon. *Journal of Sedimentary Research* **69**, 384–93.

SAID, M. & EL KELANI, A. 1988. Contribution to the geology of southeast Sinai. *26th Annual Meeting of Geological Society of Egypt, Cairo*, pp. 30–1.

SANDLER, A., TEUTSCH, N. & AVIGAD, D. 2012. Sub-Cambrian pedogenesis recorded in weathering profiles of the Arabian-Nubian Shield. *Sedimentology* **59**, 1305–20.

SCHÖNER, R. & GAUPP, R. 2005. Diagenetic mineral reactions influenced by hydrocarbon fluids: evidence from deeply buried red bed reservoirs of the Central European Basin System. *American Association of Petroleum Geologists Annual Convention and Exhibition, Calgary, Canada*, Abs. #90039.

STERN, R. J. 1994. Arc assembly and continental collision in the Neoproterozoic East African Orogen: implications for consolidation of Gondwanaland. *Annual Review of Earth and Planetary Sciences* **22**, 319–51.

SULLIVAN, M. D., HASZELDINE, R. S., BOYCE, A. J., ROGERS, G. & FALLICK, A. E. 1994. Late anhydrite cements mark basin inversion; isotopic and formation water evidence, Rotliegend Sandstone, North Sea. *Marine and Petroleum Geology* **11**, 46–54.

SUTTNER, L. J. & DUTTA, P. K. 1986. Alluvial sandstone composition and paleoclimate, I. framework mineralogy. *Journal of Sedimentary Petrology* **56**, 329–45.

TAWFIK, H. A., GHANDOUR, I. M., MAEJIMA, W. & ABDEL-HAMEED, A. T. 2010. Reservoir heterogeneity in the Cambrian sandstones: a case study from the Araba Formation, Gulf of Suez Region, Egypt. *Journal of Geoscience, Osaka City University* **53**, 1–29.

TAWFIK, H. A., GHANDOUR, I. M., MAEJIMA, W. & ABDEL-HAMEED, A. T. 2011. Petrography and geochemistry of the Lower Paleozoic Araba Formation, northern Eastern Desert, Egypt: implications for provenance, tectonic setting and weathering signature. *Journal of Geoscience, Osaka City University* **54**, 1–16.

TAWFIK, H. A., GHANDOUR, M. I., MAEJIMA, W. & ABDEL-HAMEED, A. T. 2012. Petrochemistry of the Lower Cambrian Araba Formation, Taba Area, East Sinai, Egypt. *American Association of Petroleum Geologists Annual Convention and Exhibition, Long Beach, California*, Abs. #50655.

TAYLOR, S. R. & MCLENNAN, S. M. 1985. *The Continental Crust: Its Composition and Evolution*. Oxford: Blackwell, 312 pp.

VERMA, S. P. & ARMSTRONG-ALTRIN, J. S. 2013. New multidimensional diagrams for tectonic discrimination of siliciclastic sediments and their application to Precambrian basins. *Chemical Geology* **355**, 117–33.

WEISSBROD, T. & NACHMIAS, J. 1987. Stratigraphic significance of heavy minerals in the Late Precambrian–Mesozoic clastic sequence (Nubian Sandstone) in the near east. *Sedimentary Geology* **47**, 263–91.

WEISSBROD, T. & PERATH, I. 1990. Criteria for the recognition and correlation of sandstone in the Precambrian and Paleozoic-Mesozoic clastic sequence in the near east. *Journal of African Earth Sciences* **10**, 253–70.

ZAID, S. M. 2015. Geochemistry of sandstones from the Pliocene Gabir Formation, North Marsa Alam, Red Sea, Egypt: implication for provenance, weathering and tectonic setting. *Journal of African Earth Sciences* **102**, 1–17.

ZAID, S. M., ELBADRY, O., RAMADAN, F. & MOHAMED, M. 2015. Petrography and geochemistry of Pharaonic sandstone monuments in Tall San Al Hagr, Al Sharqiya Governorate, Egypt: implications for provenance and tectonic setting. *Turkish Journal of Earth Sciences* **24**, 344–64.

ZAID, S. M. & GAHTANI, F. A. 2015. Provenance, diagenesis, tectonic setting and geochemistry of Hawkesbury sandstone (Middle Triassic), southern Sydney Basin, Australia. *Turkish Journal of Earth Sciences* **24**, 72–98.

ZIMMERMANN, U. & SPALLETTI, L. A. 2009. Provenance of the Lower Paleozoic Balcarce Formation (Tandilia System, Buenos Aires Province, Argentina): implications for paleogeographic reconstructions of SW Gondwana. *Sedimentary Geology* **219**, 7–23.